Cell

Epigenetic balance ensures mechanistic control of *MLL* amplification and rearrangement

Graphical abstract

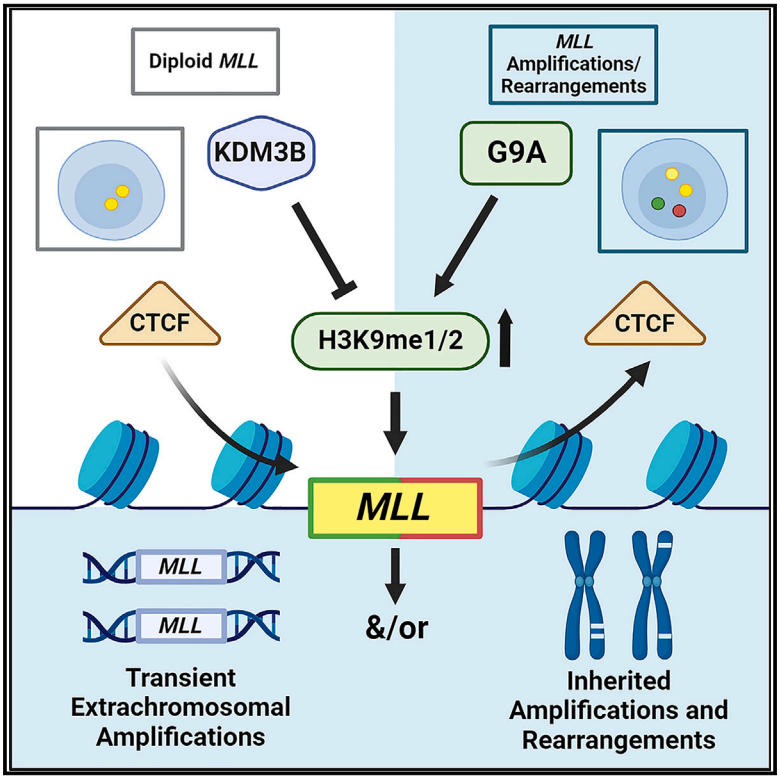

Highlights

- KDM3B and G9a regulate *MLL/KMT2A* copy gains and rearrangements through H3K9me1/2
- CTCF depletion and reduced binding associate with *KMT2A* copy gains and break aparts
- Doxorubicin reduces KDM3B and CTCF levels, promoting *MLL/KMT2A* alterations
- G9a inhibition suppresses Dox-induced *MLL/KMT2A* alterations in mice and human cells

Authors

Zach H. Gray, Damayanti Chakraborty, Reuben R. Duttweiler, ..., Hayan Lee, Ruslan I. Sadreyev, Johnathan R. Whetstine

Correspondence

johnathan.whetstine@fccc.edu

In brief

An imbalance in histone modifications contributes to both transient amplifications and integrated rearrangements and amplifications observed in leukemia, which can be induced by a commonly used chemotherapy but prevented by chemical intervention.

Gray et al., 2023, Cell *186*, 4528–4545
October 12, 2023 © 2023 Elsevier Inc.
https://doi.org/10.1016/j.cell.2023.09.009

CellPress

CellPress

Cell

Article

Epigenetic balance ensures mechanistic control of *MLL* amplification and rearrangement

Zach H. Gray,[1,2,3,11] Damayanti Chakraborty,[4,11,12] Reuben R. Duttweiler,[1,2,3,4,11] Gulnaz D. Alekbaeva,[1,2,3] Sedona E. Murphy,[4,13] Kashish Chetal,[5] Fei Ji,[5] Benjamin I. Ferman,[1,2,3] Madison A. Honer,[1,2,3] Zhentian Wang,[6,14] Cynthia Myers,[3] Renhong Sun,[7] H. Ümit Kaniskan,[7] Monika Maria Toma,[2,8] Elena A. Bondarenko,[1,2,3] John N. Santoro,[1,2,3] Christopher Miranda,[1,2,3] Megan E. Dillingham,[4,15] Ran Tang,[4,9] Or Gozani,[6] Jian Jin,[7] Tomasz Skorski,[2,8] Cihangir Duy,[1,2,3] Hayan Lee,[1,2,3] Ruslan I. Sadreyev,[5,10] and Johnathan R. Whetstine[1,2,3,4,16,*]

[1]Cancer Epigenetics Institute, Fox Chase Cancer Center, Philadelphia, PA 19111, USA
[2]Nuclear Dynamics and Cancer Program, Fox Chase Cancer Center, Philadelphia, PA 19111, USA
[3]Institute for Cancer Research, Fox Chase Cancer Center, Philadelphia, PA 19111, USA
[4]Department of Medicine, Massachusetts General Hospital Cancer Center and Harvard Medical School, Charlestown, MA 02129, USA
[5]Department of Molecular Biology, Massachusetts General Hospital, Boston, MA 02114, USA
[6]Department of Biology, Stanford University, Stanford, CA 94305, USA
[7]Mount Sinai Center for Therapeutics Discovery, Departments of Pharmacological Sciences and Oncological Sciences, Tisch Cancer Institute, Icahn School of Medicine at Mount Sinai, New York, NY 10029, USA
[8]Fels Cancer Institute for Personalized Medicine, Temple University School of Medicine, 3420 N. Broad Street, MRB 548, Philadelphia, PA 19140, USA
[9]School of Life Science and Technology, Harbin Institute of Technology, 150000 Harbin, China
[10]Department of Pathology, Massachusetts General Hospital and Harvard Medical School, Boston, MA 02114, USA
[11]These authors contributed equally
[12]Present address: Ludwig Institute for Cancer Research, University of Oxford, Oxford, UK
[13]Present address: Department of Genetics and Developmental Biology, Stanford Medicine, Stanford, CA 94305, USA
[14]Present address: Shanghai Fifth People's Hospital, Fudan University, Shanghai, China
[15]Present address: Department of Systems Biology, Harvard Medical School, Boston, MA 02115, USA
[16]Lead contact
*Correspondence: johnathan.whetstine@fccc.edu
https://doi.org/10.1016/j.cell.2023.09.009

SUMMARY

MLL/KMT2A amplifications and translocations are prevalent in infant, adult, and therapy-induced leukemia. However, the molecular contributor(s) to these alterations are unclear. Here, we demonstrate that histone H3 lysine 9 mono- and di-methylation (H3K9me1/2) balance at the *MLL/KMT2A* locus regulates these amplifications and rearrangements. This balance is controlled by the crosstalk between lysine demethylase KDM3B and methyltransferase G9a/EHMT2. KDM3B depletion increases H3K9me1/2 levels and reduces CTCF occupancy at the *MLL/KMT2A* locus, in turn promoting amplification and rearrangements. Depleting CTCF is also sufficient to generate these focal alterations. Furthermore, the chemotherapy doxorubicin (Dox), which associates with therapy-induced leukemia and promotes *MLL/KMT2A* amplifications and rearrangements, suppresses KDM3B and CTCF protein levels. KDM3B and CTCF overexpression rescues Dox-induced *MLL/KMT2A* alterations. G9a inhibition in human cells or mice also suppresses *MLL/KMT2A* events accompanying Dox treatment. Therefore, *MLL/KMT2A* amplifications and rearrangements are controlled by epigenetic regulators that are tractable drug targets, which has clinical implications.

INTRODUCTION

Genomic instability is a hallmark of cancer.[1,2] Cancer is often associated with copy number changes (e.g., gains/losses of chromosome arms and/or whole chromosomes and amplification/deletion of genomic regions) and structural rearrangements.[3] These events can be genetically stable; however, focal DNA copy gains can also be extrachromosomal, transiently appearing and disappearing based on their environment.[3–5] A key question remains as to whether the appearance of low- or high-copy extrachromosomal DNA (ecDNA) gains is associated with or precedes the integration events that result in genomic rearrangements and subsequently genetic heterogeneity.

Recent discoveries demonstrated that epigenetic regulators control transient site-specific extrachromosomal copy gains (TSSGs) of regions impacting therapeutic response and drug resistance.[3,6–10] For example, the histone 3 lysine 9/36 (H3K9/36) tri-demethylase KDM4A enzyme was shown to promote

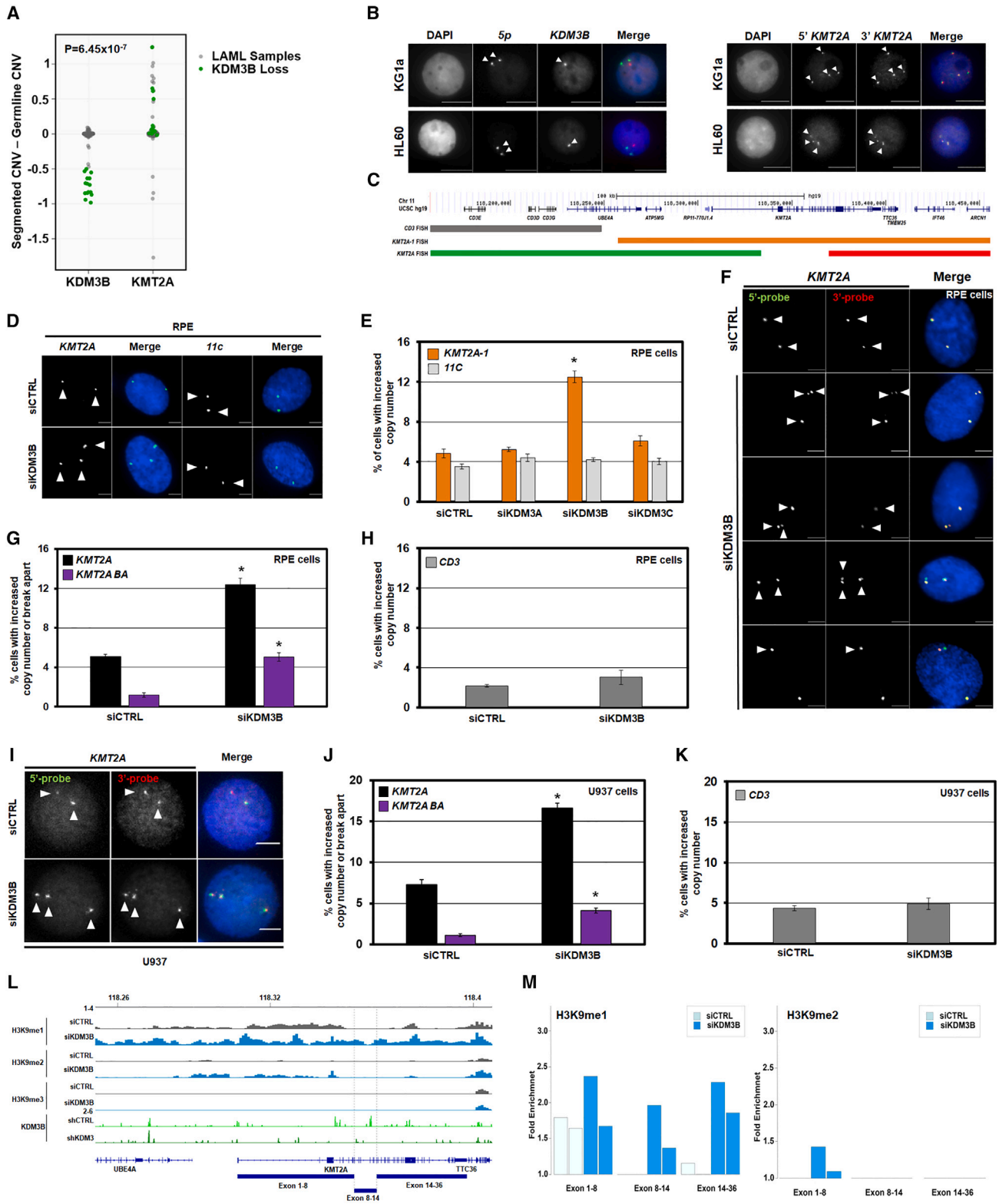

Figure 1. KDM3B depletion induces *KMT2A* DNA copy gains and break aparts

(A) Analysis of TCGA LAML samples showing most LAML samples with *KDM3B* loss also have *KMT2A* copy gain with a p value of 6.45e−7. Statistical significance was computed by Wilcoxon rank-sum test, which provides a non-parametric hypothesis test on two independent samples.

(legend continued on next page)

selective extrachromosomal TSSGs.[7] Subsequently, a collection of methyl-lysine modifying enzymes was shown to regulate these TSSGs.[9,10] These studies suggest that additional chromatin modulators could be involved in fine-tuning local and global chromatin states and regulating unknown TSSGs.

Acute myeloid leukemia (AML) and myelodysplasia (MDS) are characterized by genomic amplifications and translocations of the 11q23 region, including *MLL (Mixed-lineage leukemia 1)/KMT2A (lysine methyltransferase 2A)* and other target genes.[11–18] *MLL/KMT2A* rearrangements are observed in greater than 70% of infant leukemias,[19,20] as well as adult primary and therapy-related leukemias.[21–26] *KMT2A* rearrangements result in the fusion of the gene to more than 100 partner genes leading, to protein chimeras[26] and a number of noncoding regions throughout the genome.[26] Therapy-related AML (t-AML) is a clinical syndrome occurring long after chemotherapy treatment with agents such topoisomerase II (topo II) inhibitors.[27–29] Approximately 10% of all AML cases arise after a patient's exposure to therapy for a primary malignancy,[27] and t-AML patients have significantly worse outcomes than those who develop AML *de novo*.[27,29,30] To date, there is a clinically unmet need regarding the mechanistic understanding of how chemotherapy promotes DNA rearrangements.

The H3K9me1/2 lysine demethylase KDM3B, originally named 5qNCA, resides in the frequently deleted region of 5q31 associated with the loss of heterozygosity (LOH).[31–33] *MLL/KMT2A* copy gains often occur with 5q LOH.[34,35] KDM3B has been implicated as a myeloid leukemia tumor suppressor through oncogene regulation and contributes to genome stability; however, a full appreciation for the role KDM3B plays in genome regulation is understudied.[31,36–39] We previously reported that loss of a region on chromosome 19, containing microRNA mir-23, promoted TSSGs through KDM4A stabilization.[8] These observations prompted us to assess whether reduced KDM3B directly promotes the *MLL/KMT2A* copy gains and associated genomic insertions.

Consistent with these observations,[34,35] we demonstrate with DNA fluorescent *in situ* hybridization (FISH) that KDM3B depletion or chemical inhibition promotes transient and integrated site-specific *MLL/KMT2A* copy gains and rearrangements. These events are directly antagonized by depletion/inhibition of a H3K9me1/2 lysine methyltransferase (KMT) G9a/EHMT2. This axis controls H3K9me1/2 at *KMT2A*, especially in the region most frequently associated with genomic break aparts (BAs) and rearrangements. We further demonstrate that a KDM3B-G9a balance controls CTCF occupancy in the H3K9 methylation-enriched region and, in turn, the ability of the *KMT2A/MLL* locus to undergo site-specific copy gains and genomic rearrangement. We then establish that the chemotherapeutic agent doxorubicin (Dox) reduces KDM3B and CTCF protein levels and, as a consequence, promotes *KMT2A* copy gains and rearrangements. KDM3B overexpression rescues Dox-induced *KMT2A* changes. Furthermore, knockdown or chemical inhibition of G9a rescues *MLL/KMT2A* alterations in Dox-treated cells and mice. Collectively, these data highlight a critical role for H3K9me1/2 balance through KDM3B/G9a in regulating selective amplification and rearrangement of *KMT2A*. This discovery has major clinical implications in understanding the genesis of extrachromosomal amplifications and associated chromosomal rearrangements and sheds light on how to therapeutically control the emergence of treatment-induced *KMT2A* amplifications and rearrangements in cancer.

RESULTS

Loss of KDM3B causes site-specific copy gains of *MLL/KMT2A* locus

KDM3B is a H3K9me1/2 demethylase located in the 5q31.1 region, associated with *KMT2A* amplification and rearrangements.[31,35,37,40] To confirm this relationship, The Cancer Genome Atlas (TCGA) AML (LAML) samples containing >50% *KDM3B* loss were assessed for *KMT2A* copy number. Most samples with >50% *KDM3B* loss have *KMT2A* gains, with some showing >50% copy gain ($p = 6.45e{-}7$; Figure 1A, green dots). Furthermore, DNA FISH for *KDM3B* and *KMT2A* on leukemic cell lines with *KDM3B* LOH (KG1a and HL60) had cells within the population with an increased *KMT2A* baseline copy number (Figures 1B and 1C).

We then tested whether depletion of KDM3B and/or other KDM3 family members generates *KMT2A* copy gains and genomic structural changes. Specifically, immortalized retinal pigment epithelial (RPE) cells were siRNA depleted for each KDM3 family member.[7,10,42] These cells are ideal for assessing

(B) Representative DNA FISH with the 5qDel probe (5q probe covers *KDM3B* locus) demonstrating 5q LOH status (red) of KG1a (upper) and HL60 (lower) (left panels). Examples with *KMT2A* DNA FISH probe (C) demonstrate a baseline increase in *KMT2A* copies in KG1a (upper) and HL60 (lower) (right panels). Arrowheads highlight the FISH signal.
(C) A schematic of DNA fluorescent *in situ* hybridization (FISH) probe genomic locations that are used for *KMT2A* locus.
(D) Representative siCTRL (upper) and siKDM3B (lower) DNA FISH images with the *KMT2A-1* probe (orange probe in C and centromere 11 region [*11C*; control probe]).
(E) KDM3 family siRNA screen demonstrates that only KDM3B depletion generates *KMT2A* copy gains (*KMT2A-1*; orange) but not copy gains of centromere 11 (*11C*; gray).
(F) Representative images with the clinical *KMT2A* DNA FISH break apart probe (red and green probes in C) that show no copy gain in siCTRL (top), DNA copy gains (middle 3 panels), and break apart events (bottom) upon KDM3B siRNA depletion. Arrowheads highlight the FISH signal.
(G and H) DNA FISH showing KDM3B siRNA knockdown results in *KMT2A* copy gains (black) and break aparts (purple) but not *CD3* (gray).
(I) Representative images with the clinical *KMT2A* DNA FISH break apart probe (red and green probes in schematic C) that show *KMT2A* copy gains with siRNA-mediated KDM3B knockdown in U937 leukemia cells. Arrowheads highlight the FISH signal.
(J and K) DNA FISH showing KDM3B siRNA knockdown results in *KMT2A* copy gains and break aparts but not *CD3* alterations in U937 cells.
(L) Input-normalized H3K9me1–3 ChIP-seq tracks of the region containing *KMT2A*. Publicly available ChIP-seq shows KDM3B binding within the BCR in HCT-116 cells, which is lost upon shKDM3 treatment (green tracks).[41]
(M) Bar graphs of ChIP-seq data in (L) demonstrating increased fold enrichments of H3K9me1/2 within the *KMT2A* locus.
Error bars represent the SEM. *$p < 0.05$ by two-tailed Student's t test. Scale bar represents 5 μm. See also Figure S1.

DNA amplification and rearrangement mechanisms because they have a stable genome, do not harbor cancer mutations, and are near diploid.[7,10,42–46] Each independent set of siRNAs was validated and assessed for major cell cycle defects by flow cytometry analysis before being assayed by DNA FISH (Figures S1A–S1C). A DNA FISH probe against the *KMT2A* gene (Figure 1C; noted in orange) and a centromeric region at chromosome 11 (*11C*) were used to evaluate site-specific DNA copy gains. Copy number gain evaluation for each FISH probe was measured in percentages as previously described.[6–10]

Although KDM3 family members have comparable H3K9me1/2 activity *in vitro* (Figures S1D–S1F), only KDM3B siRNA depletion caused a significant increase in *KMT2A* copy gains with no significant changes to the *11C* control region (Figures 1D and 1E). We then assessed the site-specific impact of KDM3B depletion on *KMT2A* by leveraging a clinically relevant two-color DNA FISH probe that covers *KMT2A* (green: 5′ end of *KMT2A* and red: 3′ end of *KMT2A*) and an adjacent and partially overlapping FISH probe (called *CD3*) (Figure 1C). The dual *KMT2A* FISH probes allow both locus rearrangement (referred to as BA) and DNA copy gains to be identified. KDM3B knockdown caused a significant increase in *KMT2A* gains (black bars) and BA (purple bars) events (Figures 1F and 1G). The amplifications did not have N-terminal (green) or C-terminal (red) bias for the *KMT2A* gene, including the whole gene (both probes pseudo-colored yellow) (Figure 1F). The adjacent FISH probe *CD3* (Figure 1C, gray) did not change upon KDM3B depletion (Figure 1H), emphasizing the site-specific control of KDM3B depletion.

We then explored the specificity of KDM3B siRNA-mediated depletion in generating leukemia-associated amplifications and/or rearrangements by conducting FISH for a panel of leukemia-associated amplified and/or rearranged genes (e.g., ENL/MLLT1 and AF9/MLLT3; Figures S1G–S1O).

Most regions did not change in their basal DNA copy number, with the exception of *TCF3/E2A* and *AFF3/LAF4* (Figures S1M–S1O). We also observed *KMT2A* site-specific copy gains and rearrangements in the U937 leukemia cell line[47,48] with KDM3B depletion but not *TCF3/E2A* or *AFF3/LAF4* (Figures 1I–1K and S1P–S1R). These data suggest that unlike the *KMT2A* locus, these other regions are not consistently regulated by KDM3B across cell lines.

KDM3B depletion alters H3K9me1/2 across the *KMT2A* genomic locus

KDM3B is an H3K9me1/2 demethylase (Figures S1D–S1F).[38,49] Therefore, we performed chromatin immunoprecipitation (ChIP) sequencing (ChIP-seq) for H3K9me1/2/3 methylation marks in control and KDM3B siRNA-transfected RPE cells (Figure S1S). KDM3B depletion produced genome-wide H3K9me1 changes that were preferentially skewed toward an increase of these marks (points above the upper red line: >1.5-fold increase) (Figure S1T). The magnitude of H3K9me1 increase across the middle of the *KMT2A* gene (red points) was one of the strongest events across the genome (Figure S1T). The list of all 10 kb genomic bins with increased H3K9me1, and their nearest associated genes can be found in Table S1. A similar genome-wide increase of H3K9me2 was observed (Figure S1U).

Both H3K9me1/2 increased upon KDM3B depletion across the *KMT2A* gene body, particularly H3K9me1 within the 8.3 kb breakpoint cluster region (BCR) spanning exons 8–14, which is enriched for *KMT2A* rearrangements (Figures 1L, 1M, and S1S–S1U).[50] In control cells, H3K9me1 at BCR was lower than the adjacent regions (Figures 1L and 1M). KDM3B knockdown led to a strong increase of H3K9me1 uniformly across the BCR (Figure 1L). H3K9me2 increased on the flank to the BCR (Figures 1L and 1M). We also observed altered H3K9me1/2 at other amplified and rearranged targets *TCF3* and *AFF3* regulated by KDM3B (Figures S1T–S1W). Consistent with a direct effect of KDM3B, analysis of published KDM3B ChIP-seq data[41] demonstrated that KDM3B binds across *KMT2A*, with a strong peak within the BCR that was lost upon short hairpin (sh)RNA-mediated KDM3B depletion (Figure 1L). KDM3B also binds across *TCF3* and *AFF3* (Figures S1V and S1W). Collectively, our data establish that KDM3B depletion alters H3K9me1/2 methylation landscape of *KMT2A*, especially H3K9me1 at the BCR region, and contributes to *KMT2A* copy gains and BA events.

Inhibition or depletion of KDM3B causes inherited *KMT2A* copy gains and genomic alterations

Using a KDM3 family inhibitor (JDI-12, referred to as KDM3i),[51] we suppressed KDM3B enzymatic activity *in vitro* (Figure S2A) and noted a modest suppression of growth at 1 μM with no impact at 25 nM in RPE cells (Figure S2B). These doses were sufficient to promote significant *KMT2A* DNA copy gains and genomic rearrangements without altering KDM3B protein levels (Figures 2A, S2C, and S2D). Furthermore, KDM3B inhibition significantly increased *KMT2A* copy gains and genomic rearrangements in a panel of primary and cancer cell lines (KG1a cells, a primary AML-derived cell line, a primary AML organoid model, and primary hematopoietic stem and progenitor cells [HSPCs]; Figures 2B–2E).

KMT2A amplifications occur as both extrachromosomal and integrated events.[35,52] By adding and removing KDM3i, the transient or permanent behavior of the *KMT2A* copy gains and genomic alterations was assessed. *KMT2A* DNA copy gains and BA events occur 12 h after KDM3i treatment (Figure 2F, KDM3i 12 h) but are not observed upon KDM3i removal (Figure 2F, KDM3i 12 h washout). The total cell number was not reduced under these conditions (Figure S2E). These data suggest that KDM3B inhibition promotes transient *KMT2A* amplifications (TSSGs) and altered genomic rearrangement in a short time frame, which raises the question if longer KDM3i treatment could result in inherited DNA amplifications through insertion/rearrangement. Therefore, we treated cells for 72 h (approximately 3 cell divisions) and then passaged them into fresh media (wash-off) for additional passages, which ensured that no active drug was present before assessing *KMT2A* alterations (Figure 3A). The longer suppression resulted in both *KMT2A* copy gains and genomic rearrangements being inherited (Figure 3B), which was confirmed with DNA FISH on mitotic chromosomes (Figures 3C and 3D).

Upon transient siRNA depletion, KDM3B protein levels return to baseline levels by the third passage (P3) (Figure 3E). Inherited copy gains and genomic structure changes were still present in later passage interphase nuclei and mitotic chromosomes

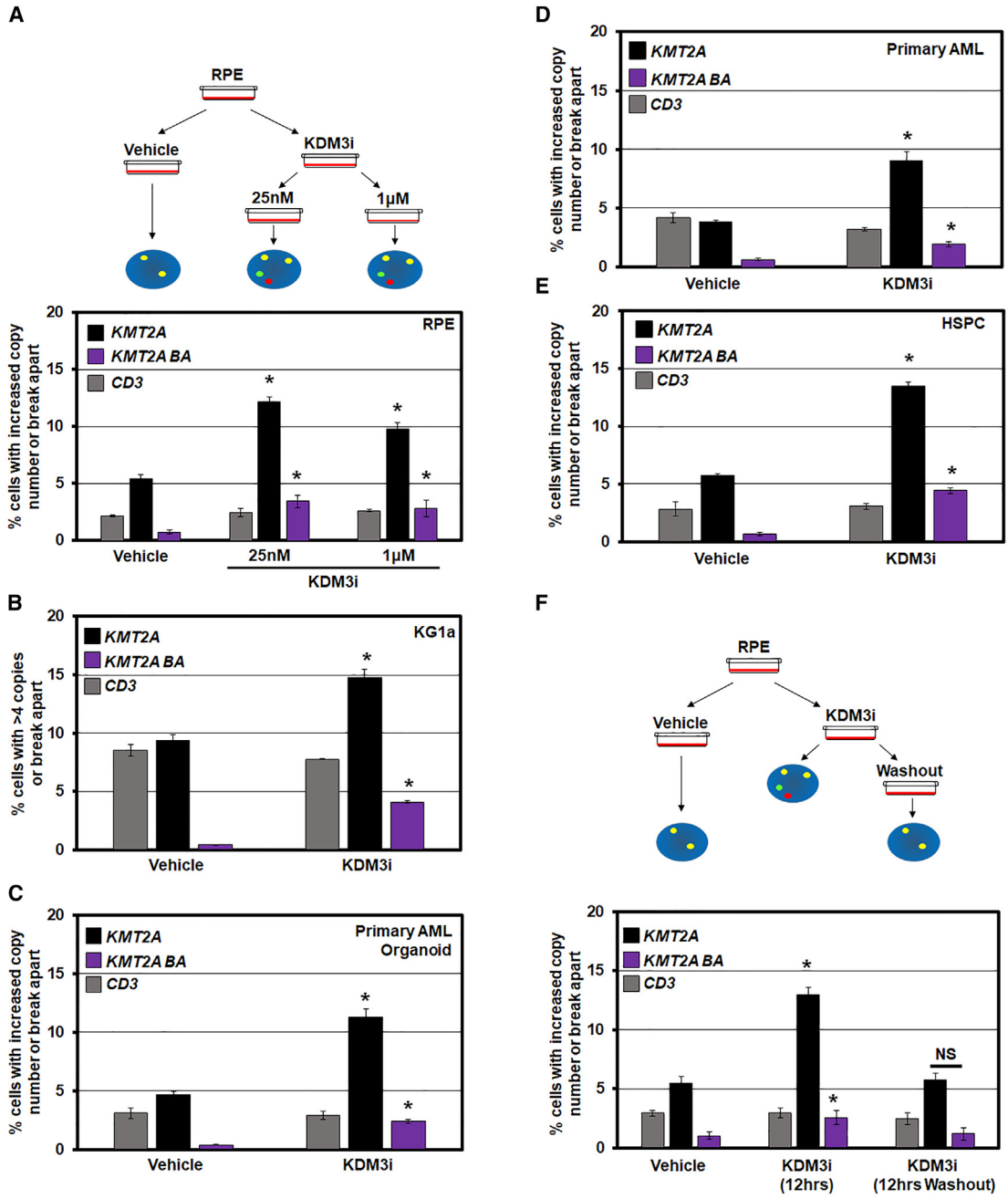

Figure 2. KDM3B chemical inhibition (KDM3i) promotes transient *KMT2A* copy gains and break aparts

(A) Schematic (top) and quantification of DNA FISH (bottom), demonstrating that *KMT2A* amplification and break apart events occur with KDM3B inhibitor treatment but no change in copy number at the adjacent *CD3* locus in RPE cells.

(B–E) DNA FISH showing that KDM3B inhibition results in *KMT2A* copy gains and break aparts in KG1a, AML organoids, primary AML cells, and hematopoietic stem and progenitor cells with no change in copy number at the *CD3* locus.

(F) Schematic (top) and quantification of DNA FISH (bottom) showing that KDM3 inhibition (KDM3i) results in *KMT2A* copy gains and break aparts. Upon KDM3i washout (12-h washout), copy gains and break aparts no longer occur. No significant change occurred with the *CD3* probe.

Error bars represent the SEM. *p < 0.05 by two-tailed Student's t test. See also Figure S2.

following siRNA-mediated KDM3B depletion; however, no change occurred to the adjacent region (Figures 3F–3H). Increased inherited copies were confirmed with a *KMT2A* digital droplet PCR (ddPCR), using the adjacent *CD3E* gene as a control (Figure S3A). Although *TCF3* copy gains were inherited, *AFF3* copy gains were not present in later passages

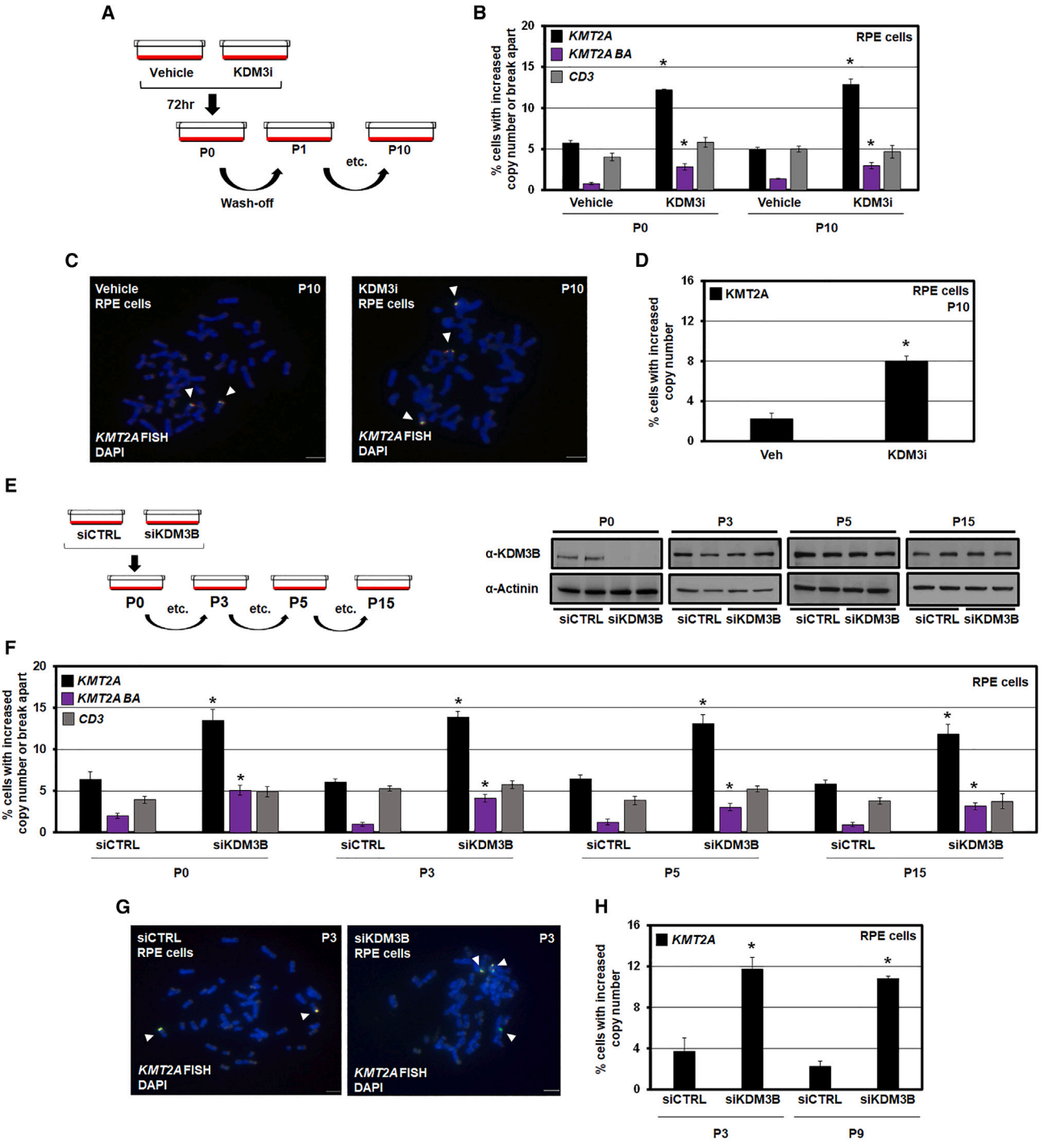

Figure 3. KDM3B suppression leads to integration and inheritance of *KMT2A* copy gains and break aparts

(A) A KDM3i treatment schematic and associated passaging of RPE cells. Cells were treated with 25 nM of KDM3i. Cells were passaged in media without KDM3i every 3 days for sequential passages.

(B) *KMT2A* and *CD3* DNA FISH at passage 0 and passage 10 after KDM3i treatment, which demonstrates *KMT2A* copy gains and break aparts are inherited in RPE cells after 10 passages (P10). No significant change occurred with the *CD3* probe.

(C) Example metaphase spreads for *KMT2A* FISH for vehicle and KDM3i-treated cells at passage 10. Arrowheads highlight the FISH signal.

(D) Quantification of the metaphase spreads with *KMT2A* FISH in KDM3i-treated cells and passage 10 cells demonstrating increased copies of *KMT2A* are retained.

(legend continued on next page)

(Figures S3B–S3D). These data demonstrate that KDM3B inhibition and depletion promote transient amplification and integrated rearrangement events with extended suppression.

G9a and KDM3B crosstalk controls *KMT2A* copy gains and rearrangements

We previously demonstrated that co-depletion of specific H3K4 KMTs with the KDM5A enzyme prevents the KDM5A-driven TSSGs.[9,10] Our results suggest that proper balance of H3K9me1/2 is critical in regulating site-specific copy gains and genomic rearrangements at *KMT2A* (Figure 1). Therefore, we pre-depleted either of the two H3K9me1/2 KMTs, G9a/EHMT2, and EHMT1,[53] before KDM3B and assessed *KMT2A* DNA copy gains or rearrangements (Figures S4A–S4D). Pre-depletion of G9a, but not EHMT1, rescued/prevented the *KMT2A* amplification and genomic alterations caused by KDM3B depletion (Figure 4A). Rescue was also observed for *TCF3* and *AFF3* copy gains (Figures S4E–S4G). Furthermore, co-treatment with KDM3i and a dual inhibitor for G9a/EHMT2 and EHMT1 (EHMT1/2 inhibition [EHMTi])[54] completely rescued *KMT2A* amplification and rearrangements with no impact on cell growth (Figures 4B and S4H). To strengthen the relationship between G9a and *KMT2A* amplification regulation, we transiently overexpressed G9a for 24 h and assessed *KMT2A* genomic alterations (Figures 4C, S4I, and S4J). G9a overexpression was sufficient to promote *KMT2A* copy gains and genomic alterations (Figure 4C), emphasizing the role of H3K9me1/2 methylation balance in regulating focal amplification of *KMT2A*.

We then hypothesized that G9a depletion could rescue the extrachromosomal amplifications caused by constantly reduced KDM3B levels. Therefore, we siRNA-depleted G9a in the KDM3B LOH leukemia cell line HL60 and evaluated whether the increased *KMT2A* copy number observed in these cells would be reduced or reset (Figure S4K). Although *KMT2A* copy gains were significantly suppressed (Figure 4D), the levels were still higher than the baseline in RPE cells, suggesting that HL60 contains both transient extrachromosomal and inherited forms. To further explore this relationship, we siRNA-depleted G9a in the *KMT2A*-inherited RPE cell lines after their level of KDM3B had returned to baseline (Figures 3E–3G) and assessed whether depletion of G9a could rescue the inherited *KMT2A* gains (Figure S4L). G9a depletion did not impact the inherited *KMT2A* copy gains (Figure 4E), suggesting that inherited extra copies are stable and unable to be rescued. Collectively, these data demonstrate that KDM3B/G9a coordinates *KMT2A* amplification and rearrangements.

Since G9a depletion rescued *KMT2A* amplifications and genomic alterations caused by KDM3B suppression (Figures 4A and 4B), we hypothesized that co-depletion of G9a with KDM3B would reset the H3K9me1/2 patterns at *KMT2A*, strengthening the importance of H3K9me1/2 balance in regulating the *KMT2A* locus. In fact, the preferential genome-wide increase of H3K9me1 and H3K9me2 caused by siKDM3B was mostly rescued by double KDM3B and G9a knockdown. H3K9me1 increase was rescued across 81% of regions genome-wide (88 Mb of the total 109 Mb), whereas H3K9me2 increase was rescued across 75% of regions genome-wide (219 Mb of the total 292 Mb) (Figure S4M). These data suggest that maintaining a KDM3B-G9a balance is critical for controlling H3K9me1/2 levels genome-wide.

G9a depletion was able to completely reset the H3K9me1 patterns at the BCR (exons 8–14) in *KMT2A* (Figures 4F, 4G, and S4N). Consistent with *KMT2A*, we also observed similar rescue at *TCF3* and *AFF3* (Figure S4N). KDM3B and G9a knockdowns produced genome-wide H3K9me1 changes with opposite preferential patterns, whereas the double knockdown rescued these skews. For example, the KDM3B knockdown (Figure S4N, left plot) resulted in a preferential increase of H3K9me1. By contrast, G9a knockdown (Figure S4N, middle plot) resulted in a decrease of H3K9me1. In the double knockdown (Figure S4N, right plot), H3K9me1 changes were strongly reduced compared with siKDM3B alone, with a smaller extent of differences from control in either direction. Similar results for G9a rescue of H3K9me2 across the genome, including *KMT2A*, *TCF3*, and *AFF3* are shown in Figure S4O. The list of all 10 kb genomic bins that had changes in H3K9me1/2 and their nearest associated genes can be found in Table S2. These data suggest that KDM3B-G9a balance controls H3K9me1/2 levels and, in turn, site-specific DNA copy gains and genomic rearrangements (Figure 4H).

Reduced CTCF occupancy promotes *KMT2A* copy gains and rearrangements

Prior studies suggest that CTCF binding could impact genome integrity, rearrangement, or duplication, especially at the *KMT2A* locus[55,56]; however, the direct role of CTCF in controlling amplification and rearrangement has not been resolved. Upon evaluating multiple cell lines and tissues from ENCODE, we observed a highly conserved occupancy for CTCF at exon 11 within the BCR of *KMT2A*, directly overlapping with KDM3B binding (Figure 5A). We hypothesized that KDM3B depletion could disrupt CTCF binding and promote *KMT2A* genomic alterations. Therefore, KDM3B and CTCF were depleted individually or in combination before assessing *KMT2A* by DNA FISH (Figures S5A and S5B). CTCF depletion alone promoted significant *KMT2A* site-specific copy gains and genomic rearrangements that were not enhanced by KDM3B depletion (Figure 5B). Since the CTCF peak within exon 11 of *KMT2A* directly overlapped with the KDM3B peak (Figure 5A), we hypothesized that

(E) A KDM3B siRNA schematic and associated passaging of RPE cells (left). Western blots for KDM3B at cell passages used for DNA FISH demonstrates KDM3B protein levels return to baseline by passage 3 (P3; right).

(F) *KMT2A* and *CD3* FISH of KDM3B siRNA-passaged cells demonstrates inheritance at passages 3, 5, and 15. No significant change occurred with the *CD3* probe at any passage.

(G) Example metaphase spreads for *KMT2A* FISH for siCTRL and siKDM3B cells at passage 3. Arrowheads highlight the FISH signal.

(H) Quantification of the metaphase spreads with *KMT2A* FISH in cells treated with siCTRL and siKDM3B from two independently propagated siCTRL and siKDM3B cells at passages 3 and 9, demonstrating increased copies of *KMT2A* are retained.

Error bars represent the SEM. *$p < 0.05$ by two-tailed Student's t test. Scale bar represents 5 μm. See also Figure S3.

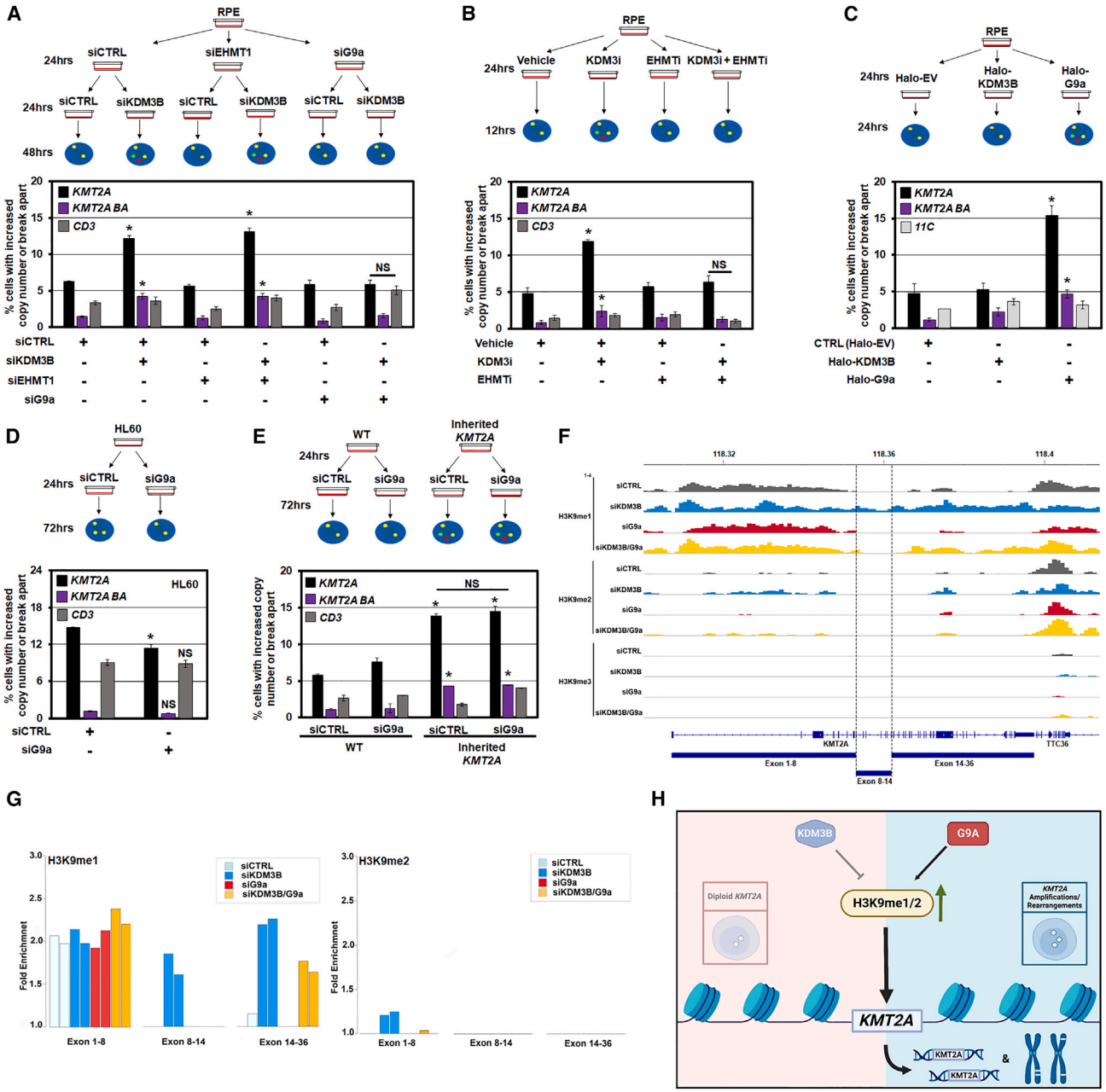

Figure 4. H3K9me1/2 balance controls *KMT2A* copy gains and break aparts

(A) A schematic (upper) and DNA FISH (lower) for co-depletion of KDM3B with EHMT1 or EHMT2/G9a. siRNA-depleted G9a but not EHMT1 prevents *KMT2A* copy gains and break aparts upon KDM3B siRNA depletion. No significant change occurred with the *CD3* probe.

(B) A schematic (upper) and DNA FISH (lower) for KDM3i and EHMTi treatment. EHMT1/2 chemical inhibition prevents *KMT2A* copy gains and break aparts upon KDM3i treatment. No significant change occurred with the *CD3* probe.

(C) A schematic (upper) and DNA FISH (lower) shows G9a overexpression promotes *KMT2A* copy gains and break aparts. Halo-EV, Halo empty vector. No significant change occurred with the *11C* probe.

(D) A schematic (upper) and DNA FISH (lower) for depletion of G9a in HL60 cells (*KDM3B* LOH cell line). G9a depletion modestly but significantly suppresses *KMT2A* copy gains in HL60 cells. No significant change occurred with the *CD3* probe.

(E) A schematic (upper) and DNA FISH (lower) for depletion of G9a in RPE-WT or RPE-inherited *KMT2A* cells. G9a depletion does not suppress *KMT2A* copy gains or break aparts in the RPE-inherited *KMT2A* cells. No significant change occurred with the *CD3* probe.

(F) Input-normalized H3K9me1/2/3 tracks at the *KMT2A* gene upon siKDM3B or siG9a alone or in combination in RPE cells.

(G) Bar graphs representing H3K9 methylation ChIP-seq fold enrichment over input in three parts of *KMT2A* gene shown in (F).

(H) A model depicting interplay between KDM3B-G9a regulating H3K9me1/2 and modulating *KMT2A* amplifications/rearrangements.

Error bars represent the SEM. *p < 0.05 by two-tailed Student's t test. NS, not significant to control. See also Figure S4.

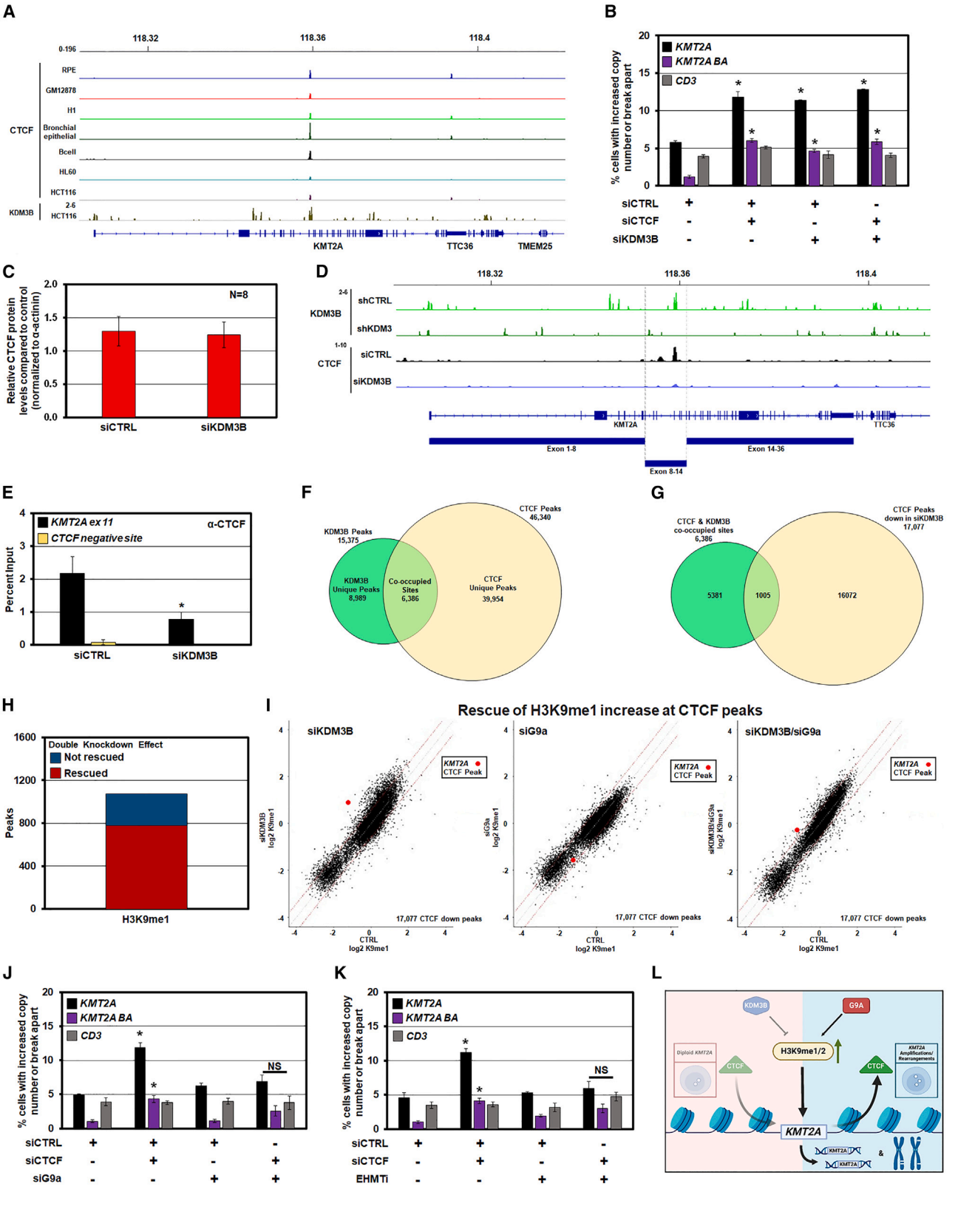

(legend on next page)

KDM3B depletion may be disrupting CTCF binding. We did not observe a global change in CTCF protein levels upon KDM3B depletion but did observe a significant reduction in CTCF binding at *KMT2A* exon 11 within the BCR by ChIP-seq and ChIP-qPCR (Figures 5C–5E and S5C).

Upon analyzing KDM3B and CTCF occupancy patterns genome-wide from public data[41] and our RPE ChIP-seq, respectively, we observed that 6,386 KDM3B peaks in the public data (41.5% of all strong KDM3B peaks) directly overlapped with the 46,340 CTCF peaks in RPE cells (p value = 1.0e−7; Figure 5F). Upon KDM3B depletion, 17,077 CTCF peaks reduced their intensity. As much as 16% of these CTCF-binding sites with reduced occupancy overlapped with KDM3B binding (1,005 peaks of the 6,386 total co-occupied sites; p value < 1.0e−216; *Z* score = 143.38) (Figure 5G). Despite the public KDM3B-binding data being from a different cell line, the association between KDM3B and CTCF binding suggests a functional interplay between KDM3B and CTCF genome-wide.

To understand the genome-wide behavior of H3K9me1 at the 17,077 CTCF-binding sites with reduced occupancy upon KDM3B depletion, we analyzed the impact of siKDM3B, siG9a, and double knockdown on the levels of H3K9me1 in the vicinity of all CTCF peaks (±5 kb flanks from the peak center). KDM3B and G9a knockdowns produced opposite changes in H3K9me1 at the CTCF proximal regions, whereas the double knockdown rescued these changes. Upon KDM3B knockdown, H3K9me1 levels increased at least 1.5-fold in the 5 kb proximity of approximately 1,000 CTCF peaks genome-wide (Figure 5H). Upon the double knockdown of KDM3B and G9a, this increase was rescued at the majority (~80%) of these peaks (Figure 5H). For example, KDM3B knockdown (Figure 5I, left plot) resulted in a preferential increase of H3K9me1 (above upper red line: >1.5-fold increase). The H3K9me1 increase at the CTCF-binding site within BCR of the *KMT2A* gene (red point) was among the strongest changes of all CTCF sites genome-wide. G9a knockdown (Figure 5I, middle plot) resulted in decreased H3K9me1 (below lower red line: >1.5-fold decrease). However, in the double KDM3B/G9a knockdown (Figure 5I, right plot), H3K9me1 changes were strongly reduced, with a smaller extent of differences from control in either direction. The level of H3K9me1 at CTCF-binding site within BCR of the KMT2A gene (red point) was close to control in the double depletion. These data indicate that KDM3B and G9a control H3K9me1/2 at CTCF peaks genome-wide, but the methylation control surrounding the *KMT2A* BCR CTCF is a strong outlier among all sites.

Since CTCF is known to regulate gene expression,[57] we assessed whether CTCF depletion regulated KDM3B expression levels. Although depletion of CTCF modestly suppressed KDM3B transcript levels (Figure S5D), both KDM3B and G9a protein levels were not significantly reduced (Figures S5E and S5G), suggesting that CTCF is a downstream effector of KDM3B loss and H3K9me1/2 disruption. We tested this by depleting or chemically inhibiting G9a in combination with CTCF depletion. G9a depletion/inhibition prevented CTCF-induced alterations (Figures 5J, 5K, and S5H–S5K). Consistent with these data, the CTCF site in the *KMT2A* BCR had increased K9me1 upon KDM3B depletion that was completely rescued upon G9a co-depletion (Figures 4F and 4G). Taken together,

Figure 5. Reduced CTCF occupancy leads to *KMT2A* copy gains and break aparts

(A) Publicly available ENCODE input-normalized ChIP-seq tracks densities of CTCF in multiple ENCODE cell lines or tissues at the *KMT2A* locus. CTCF binding at exon 11 of *KMT2A* is conserved in multiple cell lines and directly overlaps with KDM3B binding in HCT116 cells.[41]

(B) DNA FISH demonstrating single and co-siRNA depletion of KDM3B and CTCF promotes *KMT2A* copy gains and break aparts. No significant change occurred with the *CD3* probe.

(C) Quantification of western blots for CTCF in KDM3B siRNA-depleted RPE cells. No significant change in steady-state total CTCF protein levels was observed.

(D) Publicly available input-normalized ChIP-seq tracks of KDM3B[41] in control and shKDM3 cells. KDM3B binds at exon 11 and is lost upon shKDM3 (green tracks). Lower tracks: input-normalized ChIP-seq tracks of CTCF showing that siKDM3B reduced CTCF binding at exon 11 in RPE cells.

(E) ChIP-qPCR demonstrating suppression of CTCF occupancy at *KMT2A* exon 11 (*KMT2A ex 11*; black) or a negative control for CTCF binding (*CTCF negative site*; yellow) following KDM3B siRNA depletion.

(F) Venn diagram of the overlap between KDM3B ChIP-seq peaks from a public dataset and CTCF ChIP-seq peaks in this study. 6,386 of all KDM3B binding sites (41.5%) co-localize with a CTCF-binding site (p value = 1.0e−7).

(G) A total of 17,077 CTCF sites out of 46,340 (36.9%) had reduced occupancy with KDM3B depletion. Among all 6,386 KDM3B binding sites coinciding with CTCF binding, 1,005 sites show a significant decrease in CTCF binding upon KDM3B knockdown. *Z* score = 143.38, corresponding to a p value close to 0.

(H) Double KDM3B and G9a knockdown rescued the increase of H3K9me1 at the majority of CTCF peaks reduced by siKDM3B. Barplot showing genome-wide number of CTCF proximal regions (±5 kb from a CTCF peak) that decreased CTCF and increased H3K9me1 level upon KDM3B knockdown (points above upper red line in I, left scatterplot). Red, the fraction of regions where this increase was rescued by double knockdown (points moved below upper red line in I, right scatterplot).

(I) Genome-wide effects of siKDM3B, siG9a, and double knockdown on H3K9me1 levels at the subset of CTCF-binding sites where CTCF binding was decreased by siKDM3B (17,077 sites). KDM3B and G9a knockdowns have opposite skews, whereas the double knockdown strongly reduces these H3K9me1 changes. Left, scatterplot comparing input-normalized H3K9me1 ChIP-seq densities in ±5 kb proximity of all these individual CTCF peaks across the genome in control vs. siKDM3B; H3K9me1 changes are skewed toward increase (points above upper red line corresponding to >1.5-fold increase in siKM3B cells). Middle, scatterplot for control vs. siG9a cells; H3K9me1 changes are skewed toward decrease (points below lower red line corresponding to >1.5-fold decrease in siG9a cells). Right, scatterplot for control vs. siKDM3B + siG9a cells, with much fewer H3K9me1 changes in either direction. Red point, ±5-kb vicinity of CTCF-binding site within KMT2A gene.

(J) DNA FISH demonstrating siRNA depletion of G9a prevents *KMT2A* copy gains and break aparts upon CTCF siRNA depletion. No significant change occurred with the *CD3* probe.

(K) DNA FISH demonstrating EHMT1/2 chemical inhibition prevents *KMT2A* copy gains and break aparts upon CTCF siRNA depletion. No significant change occurred with the *CD3* probe.

(L) A model depicting interplay between KDM3B-G9a-CTCF upon H3K9me1/2 modulation.

Error bars represent the SEM. *p < 0.05 by two-tailed Student's t test. See also Figure S5.

these data suggest that KDM3B and G9a coordinate H3K9me1/2 levels at and around the CTCF site and, in turn, impact CTCF occupancy and the predilection of *KMT2A* to undergo amplification and genomic rearrangement (Figure 5L).

Dox promotes *KMT2A* amplification and rearrangement and reduces KDM3B and CTCF protein levels

KMT2A rearrangements are observed in pediatric and therapy-induced leukemia when conventional chemotherapy is used to treat several cancer types.[24,58,59] For example, *KMT2A* amplified and rearranged MDS and AML are generated after topo II inhibitor treatment (e.g., Dox).[29] Consistent with these clinical observations, Dox treatment promoted *KMT2A*, *AFF3*, and *TCF3* copy gains and genomic alterations with no significant impact on control regions (Figures 6A, S6A, and S6B). To reduce pleiotropic defects in RPE cells, we used lower doses of Dox (1 and 5 pg/μL). Dox also promoted *KMT2A* copy gains and rearrangements in primary HSPCs (Figure 6B). These observations are consistent with prior reports showing that the topo II inhibitor etoposide induces heterogeneous rearrangements of *KMT2A* in a variety of primary and non-primary human cells.[56,60] We then treated mixed C57BL/6-129/Sv mice with Dox before isolating their spleen and assessing *Kmt2a* copy number by DNA FISH. Consistent with the human primary HSPCs (Figure 6B), cells isolated from the spleen of mice treated with Dox had increased *Kmt2a* copy gains, with no change in the adjacent *Control 9* probe compared with control mice (Figure 6C). These data demonstrate the conserved impact of Dox treatment on site-specific *Kmt2a* copy gain events in the mice.

Since the reduction of KDM3B or CTCF levels promotes *KMT2A* copy gains and rearrangement (Figures 1, 2, 3, and 4), we assessed whether KDM3B or CTCF expression is altered upon Dox treatment. Multiple doses resulted in a significant reduction in KDM3B and CTCF transcript and protein levels in RPE cells (Figures 6D–6I); however, no change was observed with G9a transcripts (Figure S6C). We detected the same trend in KG1a cells, where Dox significantly reduced both KDM3B and CTCF transcript and protein levels (Figures 6J and S6D–S6F). Our observations are consistent with a prior report noting a loss of CTCF protein in Dox-treated patient-derived mammary epithelial cells.[61] To assess whether this was specific to Dox, we treated RPEs with another topo II inhibitor, etoposide. Consistent with Dox, etoposide significantly reduced the protein levels of KDM3B and CTCF (Figure 6K), suggesting that these effects are a result of topo II inhibition.

Previous studies have shown that Dox treatment can activate the ubiquitin-proteasome system (UPS), leading to increased protein degradation.[62] Therefore, we hypothesized that Dox could suppress KDM3B and CTCF levels through activation of the UPS. Consequently, cells were treated with Dox followed by the proteasome inhibitor MG132 before assessing KDM3B and CTCF protein levels (Figures 6L, 6M, and S6G). Treatment with Dox and MG132 partially rescued the levels of both KDM3B (Figures 6L and S6G) and CTCF (Figures 6M and S6G) compared with Dox alone. Taken together, these data emphasize that Dox regulates KDM3B and CTCF levels through both transcriptional and post-transcriptional mechanisms.

KDM3B and CTCF regulation controls Dox-induced *KMT2A* amplification and rearrangement

Since KDM3B and CTCF are reduced upon Dox treatment, the imbalance in H3K9me1/2 and CTCF occupancy at *KMT2A* could be a key driver in promoting Dox-induced *KMT2A* amplification and genomic alterations. Consistent with this relationship, Dox treatment resulted in a similar increase in H3K9me1 at the *KMT2A* CTCF site (Figures 7A, upper graph comparing siKDM3B with Dox, and S7A) and H3K9me2 at the flanking region when compared with KDM3B depletion (Figures S7A and S7B). Increased H3K9me1/2 was accompanied by reduced CTCF occupancy upon Dox treatment (Figure 7A, lower bar graph). Furthermore, CTCF overexpression was sufficient to prevent *KMT2A* copy gains upon Dox treatment (Figures 7B and S7C). CTCF overexpression appears to alter local chromosomal organization at the locus, with increased separation observed between red and green probes. Therefore, we could not assess the impact of Dox-induced rearrangements as determined by the BA events.

Since Dox reduced KDM3B levels (Figure 6) and increased H3K9me1/2 in *KMT2A* (Figure 7A), we tested whether G9a depletion would prevent Dox-induced *KMT2A* changes. *KMT2A* alterations caused by Dox were completely rescued upon G9a depletion (Figures 7C, S7D, and S7E). Furthermore, G9a inhibition significantly reduced Dox-induced *KMT2A* copy gains and prevented genomic alterations in human cells (EHMTi; Figures 7D and S7F). In addition, mice treated with EHMTi prior to Dox treatment did not generate *Kmt2a* DNA copy gains (EHMTi; Figure 7E), emphasizing the conserved importance of H3K9 methylation balance in promoting Dox-induced *KMT2A* alterations. In fact, transient KDM3B overexpression blocked *KMT2A* copy gains and rearrangements induced by Dox treatment (Figures 7F, S7G, and S7H). Collectively, these results suggest that Dox suppresses KDM3B and CTCF protein levels, which drives the copy gains and rearrangements through KDM3B/G9a imbalance and CTCF displacement, establishing a potential mechanism to therapeutically target chemotherapy-induced *KMT2A* rearrangements (Figure 7G).

DISCUSSION

This study uncovered a molecular basis for therapy-induced amplification and rearrangement of *KMT2A*. Similar observations were noted for *TCF3/E2A*, another rearranged loci in leukemia.[63–65] The findings reported in this study have broad implications because they (1) establish that epigenetic regulation controls amplification and rearrangements, (2) set the stage to discover the secondary hit(s) required for the generation of oncogenic *KMT2A* fusions, and (3) identify potential biomarkers and therapeutic targets to consider during treatments with chemotherapy and to monitor in patients post-treatment.

KDM3B depletion in relationship to *KMT2A* rearrangements and fusion partners

Currently, more than 100 known *KMT2A* rearrangement partners are documented.[26] However, not all rearrangement events generate functional fusion proteins.[66] These data suggest that the molecular mechanism(s) leading to the generation of

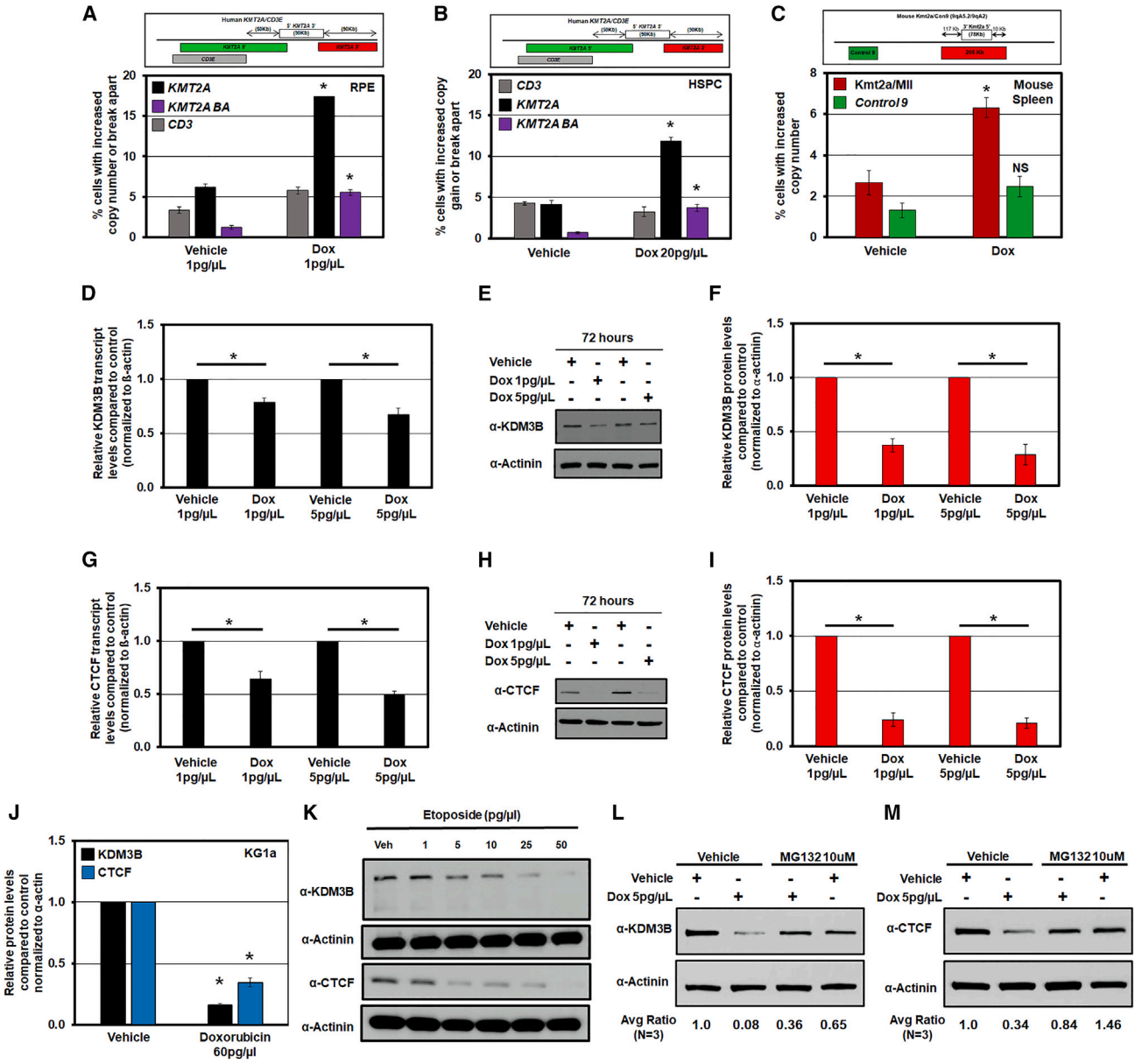

Figure 6. Doxorubicin promotes *KMT2A* amplification and rearrangement and reduces KDM3B and CTCF protein levels

(A and B) Schematic of human *KMT2A* and adjacent *CD3* DNA FISH probes (top). Graph of the DNA FISH for RPE and HSPCs treated with Dox for 72 h (bottom). Dox treatment causes significant copy gains and break aparts at the *KMT2A* locus, whereas the control region (*CD3*) changes were not significant.

(C) A schematic of DNA FISH probe genomic locations used for mouse *Kmt2a/Con9* locus (top). Graph of DNA FISH quantification demonstrating that cells isolated from the spleen of mice treated with Dox have increased copy gains of *Kmt2a* but not the adjacent *Control 9* region (bottom).

(D) Reverse transcription quantitative polymerase chain reaction (RT-qPCR) demonstrating that Dox significantly reduced KDM3B transcript levels after 72 h of exposure in RPE cells.

(E) Representative western blot illustrating Dox reducing KDM3B protein levels after 72 h of exposure in RPE cells.

(F) Quantification of western blots (n = 4) showing a significant reduction in KDM3B protein levels following Dox treatment after 72 h of exposure in RPE cells.

(G) RT-qPCR demonstrating that Dox significantly reduced CTCF transcript levels after 72 h of exposure in RPE cells.

(H) Representative western blot illustrating Dox reducing CTCF protein levels after 72 h of exposure in RPE cells.

(I) Quantification of western blots (n = 4) showing a significant reduction in CTCF protein levels following Dox treatment after 72 h of exposure in RPE cells.

(J) Graph of the quantification of western blots in Figure S6F showing a significant reduction in KDM3B (black) and CTCF (blue) protein levels following Dox treatment in KG1a cells.

(K) Western blot illustrating etoposide dose-dependently reduces KDM3B (upper) and CTCF (lower) protein levels after 72 h of exposure in RPE cells.

(L and M) Western blot illustrating MG132 partially rescues KDM3B and CTCF protein levels in the presence of Dox treatment in RPE cells. Average quantification of 3 experiments in Figure S6G are below. Protein levels were quantified using ImageJ and normalized to α-actinin.

Error bars represent the SEM. *p < 0.05 by two-tailed Student's t test. See also Figure S6.

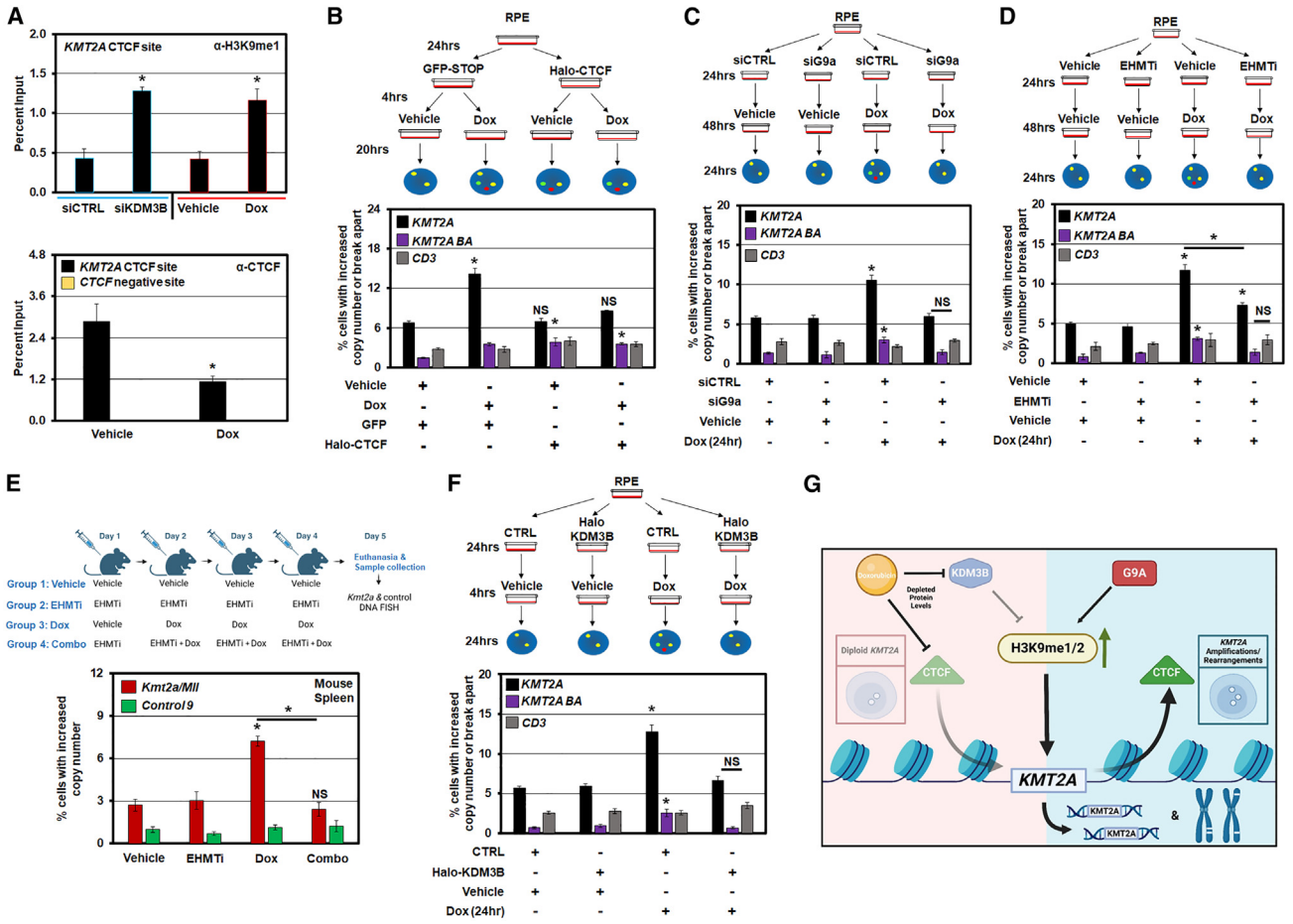

Figure 7. KDM3B and CTCF regulation controls doxorubicin-induced *KMT2A* amplification and rearrangement

(A) ChIP-qPCR demonstrating increase of H3K9me1 at *KMT2A* exon 11 (*KMT2A* CTCF site) following KDM3B siRNA depletion (left; upper) and Dox treatment at 1 pg/μL for 24 h (right; upper). ChIP-qPCR demonstrating suppression of CTCF occupancy at *KMT2A* exon 11 (*KMT2A ex 11*; black) or a negative control for CTCF binding (*CTCF negative site*; yellow) following Dox treatment at 1 pg/μL for 24 h (lower).

(B) Treatment schematic (upper) and DNA FISH (lower) demonstrating that Dox treatment causes *KMT2A* amplification and rearrangements. CTCF overexpression significantly rescues *KMT2A* amplifications.

(C) Treatment schematic (upper) and DNA FISH (lower) demonstrating that Dox treatment causes *KMT2A* amplification and rearrangement. G9a depletion significantly rescues *KMT2A* amplifications and rearrangements.

(D) Treatment schematic (upper) and DNA FISH (lower) demonstrating that Dox treatment causes *KMT2A* amplification and rearrangements that are significantly rescued with EHMT1/2 inhibition (EHMTi).

(E) Treatment schematic (upper) and DNA FISH (lower) demonstrating that Dox treatment causes *Kmt2a* copy gains in mouse cells isolated from the spleen; however, pretreatment with EHMT1/2 inhibitor (EHMTi) blocked the Dox-induced *Kmt2a* copy gains. The control region on chr9 had no significant changes with any condition (*Control 9*).

(F) Treatment schematic (upper) and DNA FISH (lower) demonstrating that Dox treatment causes *KMT2A* amplification and rearrangements that are significantly rescued with KDM3B overexpression.

(G) Model summarizing the data from Figures 1, 2, 3, 4, 5, and 6 as well as this figure. The model illustrates that KDM3B and CTCF are suppressed with Dox treatment, leading to increased H3K9 mono- and di-methylation and reducing CTCF occupancy, which in turn promotes *KMT2A* amplification and rearrangements (BA). G9a is critical in promoting *KMT2A* copy gains and rearrangements.

Error bars represent the SEM. *p < 0.05 by two-tailed Student's t test. See also Figure S7.

KMT2A rearrangements, including those that do not generate translatable products, could be key to understanding tumors containing amplifications and rearrangements.

Based on our data, it is unlikely that KDM3B loss alone provides a major cellular fitness advantage for the inherited rearranged over the non-rearranged cells. This observation is not surprising since therapy-related AML has a latency period of up to 15 years after initial treatment with chemotherapy.[29] These data suggest that KDM3B suppression or loss alone is likely just the first step necessary to promote or allow selection of the rearrangement events resulting in functional fusion proteins providing a cellular growth advantage. Studies show that non-homologous end-joining is required for topo II inhibitor-driven leukemia-associated *KMT2A* rearrangements,[56,67]

suggesting that mis-regulated DNA damage response is another possible factor involved in generating/selecting for the leukemia-associated fusion events. However, additional influences could also potentiate the driver fusion events to emerge: cellular aging, stress exposures, and/or acquired mutations.

KDM3B, 5q, and *KMT2A* amplification and rearrangements

Not all del(5q) regions contain *KDM3B*.[68] However, patients with del(5q) alone have a better prognosis compared with those presenting with del(5q) as well as other mutations or abnormalities.[69] We suspect that additional gene mutations and/or the dysregulation of additional epigenetic regulators are likely required to promote copy gains and rearrangements of the oncogenic fusion partners, providing the secondary hit(s) necessary. Furthermore, a number of other candidate tumor-suppressor genes have been identified within the del(5q) region, which may also play an oncogenic role that is independent of generating *KMT2A* amplifications and rearrangements.[33,70,71]

Epigenetics, amplification, and, in turn, rearrangements

When KDM3B was inhibited for short time intervals, the expected amplifications and BAs at *KMT2A* locus were observed but resolved quickly with drug removal, highlighting their transient extrachromosomal nature (Figure S7I). However, upon longer treatment, these genomic events become inherited and are observed on the same chromosome or other chromosomes (Figures 3 and S7I). These data illustrate that the aberrant regulation of the epigenome promotes transient DNA amplifications that can be inherited when the stimuli are maintained through multiple cell divisions (Figure S7I). Therefore, we speculate that sustained amplification and BAs are likely being incorporated into the genome through DNA damage repair pathways. Our data are consistent with those of the prior proposed mechanisms.[72] Future studies need to determine the exact integration sites and build complete sequence maps to identify the molecular features and pathways affiliated with the inherited amplifications. This study has now generated the roadmap to investigate these inherited genomic events.

Longer inhibition of KDM3B did not further increase the percent of cells within the population containing *KMT2A* alterations compared with short treatment (Figures 2 and 3). However, when inherited-*KMT2A* cell lines were exposed to KDM3i for a short time (3 and 6 h), a significant increase in *KMT2A* copy gains compared with the inherited baseline was observed (Figure S7J). Upon longer treatment (12 h), *KMT2A* copy gains returned to baseline, suggesting that those cells containing genomic aberrations of *KMT2A* are being negatively selected for, although a new population of cells with these aberrations emerge. This model is supported by increased Annexin V in the inherited-*KMT2A* cell lines treated with KDM3i at the later time points (6 and 12 h; Figure S7K). Consistent with a prior study,[51] these data suggest that *KMT2A*-rearranged cells have increased susceptibility to KDM3B inhibition. This sensitivity provides a promising therapeutic window in *KMT2A*-rearranged cancers.

KDM3B and CTCF as a bridge to Dox-induced *KMT2A* amplification and rearrangement

Upon topo II inhibitor treatment (e.g., Dox), MDS and AML occur and are accompanied by amplification and rearrangement of the *KMT2A* locus.[29] Topo II inhibitors promote non-leukemia and leukemia-associated *KMT2A* rearrangements in various cell types,[56,60] suggesting a universal regulatory mechanism controlling *KMT2A* alterations. A population-based study demonstrated that younger individuals developing secondary leukemia have a significantly worse prognosis compared with *de novo*.[73] Therefore, preventing the emergence of secondary cancer caused by chemotherapy would have a profound clinical impact. This study demonstrates that epigenetic therapies could provide a much-needed tool to combat these cancers. Furthermore, we establish the possibility of controlling chemo-induced *KMT2A* amplification and rearrangements by pretreating or co-treating patients receiving these therapies with a G9a inhibitor or CTCF/KDM3B agonist. Collectively, these observations provide a molecular basis to develop treatment protocols to prevent therapy-associated *KMT2A* rearrangements by targeting epigenetic regulators.

Limitations of the study

Our findings establish that epigenetic mechanisms control the amplification and genomic rearrangements of *KMT2A*. We demonstrate that these events are directly promoted by Dox through the suppression of KDM3B and CTCF protein levels and can be blocked by co-depletion or inhibition of G9a/EHMT2. We also show that Dox suppresses KDM3B and CTCF protein levels through transcriptional and post-transcriptional mechanisms. However, our study does not (1) demonstrate the exact mechanism by which oncogenic *KMT2A* rearrangements are generated leading to leukemia development or (2) demonstrate exactly how Dox suppresses KDM3B and CTCF protein levels. Although we have discovered the first hit required to generate leukemia-associated *KMT2A* rearrangements, the additional hit(s) required could be additional epigenetics perturbations, cellular aging, stress exposures, acquired mutations, or alterations to DNA damage repair pathways. Future studies are needed to (1) systematically test the ability to promote oncogenic *KMT2A* fusion events driving leukemia and (2) discover the exact mechanisms by which Dox suppresses KDM3B and CTCF protein levels.

STAR★METHODS

Detailed methods are provided in the online version of this paper and include the following:

- KEY RESOURCES TABLE
- RESOURCE AVAILABILITY
  - Lead contact
  - Materials availability
  - Data and code availability
- EXPERIMENTAL MODEL AND STUDY PARTICIPANT DETAILS
  - Cell Culture
  - Isolation of HSPCs
  - Mouse Model Details

- METHOD DETAILS
  - Transfection Procedure for RPE cells
  - Transfection procedure for U937, HL60 and KG1a cells
  - Long-term passage of siRNA transfected cells
  - RNA extraction and quantitative real-time PCR
  - Immunoblotting
  - Cell Cycle Analysis
  - DNA Fluorescent *In Situ* Hybridization (FISH)
  - Metaphase Spreads
  - Protein purification
  - Histone demethylase reactions
  - Digital Droplet PCR
  - Drug Treatment Conditions
  - Chromatin Immunoprecipitation
  - *In vivo* Doxorubicin
  - Annexin V Staining
- QUANTIFICATION AND STATISTICAL ANALYSIS
  - DNA FISH quantification
  - ChIP-seq analysis
  - Genome-Wide analysis of CTCF peaks

SUPPLEMENTAL INFORMATION

Supplemental information can be found online at https://doi.org/10.1016/j.cell.2023.09.009.

ACKNOWLEDGMENTS

We would like to thank the glass washing, cell culture, genomics resource, and cell sorting facilities at Fox Chase Cancer Center for support. We also thank Dr. Thomas L. Clarke for technical assistance and Drs. Capucine Van Rechem, Alfonso Bellacosa, Jon Chernoff, Jade Wilson, and Ethan Sumner for comments on the manuscript. Work related to this study is supported by R01GM097360 and R35GM144131 (J.R.W.), NIH/NCI Cancer Center support grant P30 CA006927 (J.R.W.), and the American Lung Association Lung Cancer Discovery Award (J.R.W.). O.G. is supported by NIH (R35 GM139569). D.C. is a recipient of the Ovarian Cancer Research Fund Alliance (Ann and Sol Schreiber Mentored Investigator Award-543667). B.I.F. is supported by NIH (T32 GM142606). T.S. is supported by NIH (R01 CA244044 and R01 CA237386). C.D. is supported by the V Foundation (V2021-017) and the W.W. Smith Charitable Trust (C2101). R.I.S. is supported by NIH (P30 DK040561).

AUTHOR CONTRIBUTIONS

J.R.W., Z.H.G., D.C., and R.R.D. wrote the manuscript with input from authors. J.R.W. conceived the study and associated concepts. J.R.W., Z.H.G., D.C., and R.R.D. conceptualized and designed the majority of the experiments. Z.H.G., D.C., R.R.D., G.D.A., S.E.M., K.C., F.J., B.I.F., M.A.H., Z.W., C. Myers, C.D., H.L., R.S., H.Ü.K., M.M.T., E.A.B., J.N.S., C. Miranda, M.E.D., R.T., O.G., J.J., and T.S. contributed to and/or conducted experiments and their interpretation within the manuscript. K.C., F.J., and R.I.S. designed and conducted the epigenomic computational analyses. H.L. conducted the TCGA analyses.

DECLARATION OF INTERESTS

J.R.W. has served or is serving as a consultant or advisor for Qsonica, Salarius Pharmaceuticals, Daiichi Sankyo, Inc., Vyne Therapeutics, and Lily Asia Ventures. J.R.W. also receives funding for research from Salarius Pharmaceuticals and Oryzon Genomics. O.G. is a scientific cofounder and shareholder of EpiCypher, Inc., K36 Therapeutics, Inc., and Alternative Bio, Inc. J.J. received research funds from Celgene Corporation, Levo Therapeutics, Inc., Cullgen, Inc., and Cullinan Oncology, Inc. J.J. is a cofounder and equity shareholder in Cullgen, Inc., a scientific cofounder and scientific advisory board member of Onsero Therapeutics, Inc., and a consultant for Cullgen, Inc., EpiCypher, Inc., and Accent Therapeutics, Inc. C.D. receives research funds from Janssen outside the submitted work.

Received: August 4, 2022
Revised: June 1, 2023
Accepted: September 8, 2023
Published: October 2, 2023

REFERENCES

1. Hanahan, D. (2022). Hallmarks of cancer: new dimensions. Cancer Discov. *12*, 31–46. https://doi.org/10.1158/2159-8290.CD-21-1059.
2. Hanahan, D., and Weinberg, R.A. (2011). Hallmarks of cancer: the next generation. Cell *144*, 646–674. https://doi.org/10.1016/j.cell.2011.02.013.
3. Mishra, S., and Whetstine, J.R. (2016). Different facets of copy number changes: permanent, transient, and adaptive. Mol. Cell. Biol. *36*, 1050–1063. https://doi.org/10.1128/MCB.00652-15.
4. Bailey, C., Shoura, M.J., Mischel, P.S., and Swanton, C. (2020). Extrachromosomal DNA-relieving heredity constraints, accelerating tumour evolution. Ann. Oncol. *31*, 884–893. https://doi.org/10.1016/j.annonc.2020.03.303.
5. Song, K., Minami, J.K., Huang, A., Dehkordi, S.R., Lomeli, S.H., Luebeck, J., Goodman, M.H., Moriceau, G., Krijgsman, O., Dharanipragada, P., et al. (2022). Plasticity of extrachromosomal and intrachromosomal BRAF amplifications in overcoming targeted therapy dosage challenges. Cancer Discov. *12*, 1046–1069. https://doi.org/10.1158/2159-8290.CD-20-0936.
6. Black, J.C., Atabakhsh, E., Kim, J., Biette, K.M., Van Rechem, C., Ladd, B., Burrowes, P.D., Donado, C., Mattoo, H., Kleinstiver, B.P., et al. (2015). Hypoxia drives transient site-specific copy gain and drug-resistant gene expression. Genes Dev. *29*, 1018–1031. https://doi.org/10.1101/gad.259796.115.
7. Black, J.C., Manning, A.L., Van Rechem, C., Kim, J., Ladd, B., Cho, J., Pineda, C.M., Murphy, N., Daniels, D.L., Montagna, C., et al. (2013). KDM4A lysine demethylase induces site-specific copy gain and rereplication of regions amplified in tumors. Cell *154*, 541–555. https://doi.org/10.1016/j.cell.2013.06.051.
8. Black, J.C., Zhang, H., Kim, J., Getz, G., and Whetstine, J.R. (2016). Regulation of transient site-specific copy gain by microRNA. J. Biol. Chem. *291*, 4862–4871. https://doi.org/10.1074/jbc.M115.711648.
9. Clarke, T.L., Tang, R., Chakraborty, D., Van Rechem, C., Ji, F., Mishra, S., Ma, A., Kaniskan, H.Ü., Jin, J., Lawrence, M.S., et al. (2020). Histone lysine methylation dynamics control EGFR DNA copy-number amplification. Cancer Discov. *10*, 306–325. https://doi.org/10.1158/2159-8290.CD-19-0463.
10. Mishra, S., Van Rechem, C., Pal, S., Clarke, T.L., Chakraborty, D., Mahan, S.D., Black, J.C., Murphy, S.E., Lawrence, M.S., Daniels, D.L., and Whetstine, J.R. (2018). Cross-talk between lysine-modifying enzymes controls site-specific DNA amplifications. Cell *174*, 803–817.e16. https://doi.org/10.1016/j.cell.2018.06.018.
11. Schichman, S.A., Caligiuri, M.A., Gu, Y., Strout, M.P., Canaani, E., Bloomfield, C.D., and Croce, C.M. (1994). ALL-1 partial duplication in acute leukemia. Proc. Natl. Acad. Sci. USA *91*, 6236–6239.
12. Poppe, B., Vandesompele, J., Schoch, C., Lindvall, C., Mrozek, K., Bloomfield, C.D., Beverloo, H.B., Michaux, L., Dastugue, N., Herens, C., et al. (2004). Expression analyses identify MLL as a prominent target of 11q23 amplification and support an etiologic role for MLL gain of function in myeloid malignancies. Blood *103*, 229–235. https://doi.org/10.1182/blood-2003-06-2163.
13. Walter, M.J., Payton, J.E., Ries, R.E., Shannon, W.D., Deshmukh, H., Zhao, Y., Baty, J., Heath, S., Westervelt, P., Watson, M.A., et al. (2009). Acquired copy number alterations in adult acute myeloid leukemia genomes.

Proc. Natl. Acad. Sci. USA *106*, 12950–12955. https://doi.org/10.1073/pnas.0903091106.

14. Tang, G., DiNardo, C., Zhang, L., Ravandi, F., Khoury, J.D., Huh, Y.O., Muzzafar, T., Medeiros, L.J., Wang, S.A., and Bueso-Ramos, C.E. (2015). MLL gene amplification in acute myeloid leukemia and myelodysplastic syndromes is associated with characteristic clinicopathological findings and TP53 gene mutation. Hum. Pathol. *46*, 65–73. https://doi.org/10.1016/j.humpath.2014.09.008.
15. Dolan, M., McGlennen, R.C., and Hirsch, B. (2002). MLL amplification in myeloid malignancies: clinical, molecular, and cytogenetic findings. Cancer Genet. Cytogenet. *134*, 93–101.
16. Maitta, R.W., Cannizzaro, L.A., and Ramesh, K.H. (2009). Association of MLL amplification with poor outcome in acute myeloid leukemia. Cancer Genet. Cytogenet. *192*, 40–43. https://doi.org/10.1016/j.cancergencyto.2009.02.018.
17. Cox, M.C., Panetta, P., Venditti, A., Del Poeta, G., Maurillo, L., Tamburini, A., Del Principe, M.I., and Amadori, S. (2003). Fluorescence in situ hybridization and conventional cytogenetics for the diagnosis of 11q23+/MLL+ translocation in leukaemia. Br. J. Haematol. *121*, 953–955.
18. Sperling, A.S., Gibson, C.J., and Ebert, B.L. (2017). The genetics of myelodysplastic syndrome: from clonal haematopoiesis to secondary leukaemia. Nat. Rev. Cancer *17*, 5–19. https://doi.org/10.1038/nrc.2016.112.
19. Woo, J.S., Alberti, M.O., and Tirado, C.A. (2014). Childhood B-acute lymphoblastic leukemia: a genetic update. Exp. Hematol. Oncol. *3*, 16. https://doi.org/10.1186/2162-3619-3-16.
20. Rice, S., and Roy, A. (2020). MLL-rearranged infant leukaemia: A 'thorn in the side' of a remarkable success story. Biochim. Biophys. Acta Gene Regul. Mech. *1863*, 194564. https://doi.org/10.1016/j.bbagrm.2020.194564.
21. Winters, A.C., and Bernt, K.M. (2017). MLL-rearranged leukemias-an update on science and clinical approaches. Front. Pediatr. *5*, 4. https://doi.org/10.3389/fped.2017.00004.
22. Super, H.J., McCabe, N.R., Thirman, M.J., Larson, R.A., Le Beau, M.M., Pedersen-Bjergaard, J., Philip, P., Diaz, M.O., and Rowley, J.D. (1993). Rearrangements of the MLL gene in therapy-related acute myeloid leukemia in patients previously treated with agents targeting DNA-topoisomerase II. Blood *82*, 3705–3711.
23. Andersen, M.K., Christiansen, D.H., Jensen, B.A., Ernst, P., Hauge, G., and Pedersen-Bjergaard, J. (2001). Therapy-related acute lymphoblastic leukaemia with MLL rearrangements following DNA topoisomerase II inhibitors, an increasing problem: report on two new cases and review of the literature since 1992. Br. J. Haematol. *114*, 539–543.
24. Pedersen-Bjergaard, J., Andersen, M.K., and Johansson, B. (1998). Balanced chromosome aberrations in leukemias following chemotherapy with DNA-topoisomerase II inhibitors. J. Clin. Oncol. *16*, 1897–1898. https://doi.org/10.1200/JCO.1998.16.5.1897.
25. Dulak, A.M., Schumacher, S.E., van Lieshout, J., Imamura, Y., Fox, C., Shim, B., Ramos, A.H., Saksena, G., Baca, S.C., Baselga, J., et al. (2012). Gastrointestinal adenocarcinomas of the esophagus, stomach, and colon exhibit distinct patterns of genome instability and oncogenesis. Cancer Res. *72*, 4383–4393. https://doi.org/10.1158/0008-5472.CAN-11-3893.
26. Meyer, C., Larghero, P., Almeida Lopes, B., Burmeister, T., Gröger, D., Sutton, R., Venn, N.C., Cazzaniga, G., Corral Abascal, L., Tsaur, G., et al. (2023). The KMT2A recombinome of acute leukemias in 2023. Leukemia *37*, 988–1005. https://doi.org/10.1038/s41375-023-01877-1.
27. Leone, G., Mele, L., Pulsoni, A., Equitani, F., and Pagano, L. (1999). The incidence of secondary leukemias. Haematologica *84*, 937–945.
28. Campo, E., Swerdlow, S.H., Harris, N.L., Pileri, S., Stein, H., and Jaffe, E.S. (2011). The 2008 WHO classification of lymphoid neoplasms and beyond: evolving concepts and practical applications. Blood *117*, 5019–5032. https://doi.org/10.1182/blood-2011-01-293050.
29. Godley, L.A., and Larson, R.A. (2008). Therapy-related myeloid leukemia. Semin. Oncol. *35*, 418–429. https://doi.org/10.1053/j.seminoncol.2008.04.012.
30. Borthakur, G., and Estey, A.E. (2007). Therapy-related acute myelogenous leukemia and myelodysplastic syndrome. Curr. Oncol. Rep. *9*, 373–377. https://doi.org/10.1007/s11912-007-0050-z.
31. Hu, Z., Gomes, I., Horrigan, S.K., Kravarusic, J., Mar, B., Arbieva, Z., Chyna, B., Fulton, N., Edassery, S., Raza, A., and Westbrook, C.A. (2001). A novel nuclear protein, 5qNCA (LOC51780) is a candidate for the myeloid leukemia tumor suppressor gene on chromosome 5 band q31. Oncogene *20*, 6946–6954. https://doi.org/10.1038/sj.onc.1204850.
32. Yoo, J., Jeon, Y.H., Cho, H.Y., Lee, S.W., Kim, G.W., Lee, D.H., and Kwon, S.H. (2020). Advances in histone demethylase KDM3A as a cancer therapeutic target. Cancers (Basel) *12*, 1098. https://doi.org/10.3390/cancers12051098.
33. Ebert, B.L. (2010). Genetic deletions in AML and MDS. Best Pract. Res. Clin. Haematol. *23*, 457–461. https://doi.org/10.1016/j.beha.2010.09.006.
34. Schoch, C., Kern, W., Kohlmann, A., Hiddemann, W., Schnittger, S., and Haferlach, T. (2005). Acute myeloid leukemia with a complex aberrant karyotype is a distinct biological entity characterized by genomic imbalances and a specific gene expression profile. Genes Chromosomes Cancer *43*, 227–238. https://doi.org/10.1002/gcc.20193.
35. Herry, A., Douet-Guilbert, N., Guéganic, N., Morel, F., Le Bris, M.J., Berthou, C., and De Braekeleer, M. (2006). Del(5q) and MLL amplification in homogeneously staining region in acute myeloblastic leukemia: a recurrent cytogenetic association. Ann. Hematol. *85*, 244–249. https://doi.org/10.1007/s00277-005-0059-z.
36. MacKinnon, R.N., Kannourakis, G., Wall, M., and Campbell, L.J. (2011). A cryptic deletion in 5q31.2 provides further evidence for a minimally deleted region in myelodysplastic syndromes. Cancer Genet. *204*, 187–194. https://doi.org/10.1016/j.cancergen.2011.02.001.
37. Xu, X., Nagel, S., Quentmeier, H., Wang, Z., Pommerenke, C., Dirks, W.G., Macleod, R.A.F., Drexler, H.G., and Hu, Z. (2018). KDM3B shows tumor-suppressive activity and transcriptionally regulates HOXA1 through retinoic acid response elements in acute myeloid leukemia. Leuk. Lymphoma *59*, 204–213. https://doi.org/10.1080/10428194.2017.1324156.
38. Kim, J.Y., Kim, K.B., Eom, G.H., Choe, N., Kee, H.J., Son, H.J., Oh, S.T., Kim, D.W., Pak, J.H., Baek, H.J., et al. (2012). KDM3B is the H3K9 demethylase involved in transcriptional activation of lmo2 in leukemia. Mol. Cell. Biol. *32*, 2917–2933. https://doi.org/10.1128/MCB.00133-12.
39. Saavedra, F., Gurard-Levin, Z.A., Rojas-Villalobos, C., Vassias, I., Quatrini, R., Almouzni, G., and Loyola, A. (2020). JMJD1B, a novel player in histone H3 and H4 processing to ensure genome stability. Epigenetics Chromatin *13*, 6. https://doi.org/10.1186/s13072-020-00331-1.
40. Zatkova, A., Merk, S., Wendehack, M., Bilban, M., Muzik, E.M., Muradyan, A., Haferlach, C., Haferlach, T., Wimmer, K., Fonatsch, C., et al. (2009). AML/MDS with 11q/MLL amplification show characteristic gene expression signature and interplay of DNA copy number changes. Genes Chromosomes Cancer *48*, 510–520. https://doi.org/10.1002/gcc.20658.
41. Li, J., Yu, B., Deng, P., Cheng, Y., Yu, Y., Kevork, K., Ramadoss, S., Ding, X., Li, X., and Wang, C.-Y. (2017). KDM3 epigenetically controls tumorigenic potentials of human colorectal cancer stem cells through Wnt/β-catenin signalling. Nat. Commun. *8*, 15146. https://doi.org/10.1038/ncomms15146.
42. Jiang, X.R., Jimenez, G., Chang, E., Frolkis, M., Kusler, B., Sage, M., Beeche, M., Bodnar, A.G., Wahl, G.M., Tlsty, T.D., and Chiu, C.P. (1999). Telomerase expression in human somatic cells does not induce changes associated with a transformed phenotype. Nat. Genet. *21*, 111–114.
43. Janssen, A., van der Burg, M., Szuhai, K., Kops, G.J., and Medema, R.H. (2011). Chromosome segregation errors as a cause of DNA damage and structural chromosome aberrations. Science *333*, 1895–1898. https://doi.org/10.1126/science.1210214.

44. Maciejowski, J., Li, Y., Bosco, N., Campbell, P.J., and de Lange, T. (2015). Chromothripsis and kataegis induced by telomere crisis. Cell *163*, 1641–1654. https://doi.org/10.1016/j.cell.2015.11.054.

45. Mardin, B.R., Drainas, A.P., Waszak, S.M., Weischenfeldt, J., Isokane, M., Stütz, A.M., Raeder, B., Efthymiopoulos, T., Buccitelli, C., Segura-Wang, M., et al. (2015). A cell-based model system links chromothripsis with hyperploidy. Mol. Syst. Biol. *11*, 828. https://doi.org/10.15252/msb.20156505.

46. Zhang, C.Z., Spektor, A., Cornils, H., Francis, J.M., Jackson, E.K., Liu, S., Meyerson, M., and Pellman, D. (2015). Chromothripsis from DNA damage in micronuclei. Nature *522*, 179–184. https://doi.org/10.1038/nature14493.

47. de Necochea-Campion, R., Diaz Osterman, C.J., Hsu, H.W., Fan, J., Mirshahidi, S., Wall, N.R., and Chen, C.S. (2015). AML sensitivity to YM155 is modulated through AKT and Mcl-1. Cancer Lett. *366*, 44–51. https://doi.org/10.1016/j.canlet.2015.05.034.

48. Sánchez-Reyes, K., Pedraza-Brindis, E.J., Hernández-Flores, G., Bravo-Cuellar, A., López-López, B.A., Rosas-González, V.C., and Ortiz-Lazareno, P.C. (2019). The supernatant of cervical carcinoma cells lines induces a decrease in phosphorylation of STAT-1 and NF-κB transcription factors associated with changes in profiles of cytokines and growth factors in macrophages derived from U937 cells. Innate Immun. *25*, 344–355. https://doi.org/10.1177/1753425919848841.

49. Wang, X., Fan, H., Xu, C., Jiang, G., Wang, H., and Zhang, J. (2019). KDM3B suppresses APL progression by restricting chromatin accessibility and facilitating the ATRA-mediated degradation of PML/RARalpha. Cancer Cell Int. *19*, 256. https://doi.org/10.1186/s12935-019-0979-7.

50. Broeker, P.L., Super, H.G., Thirman, M.J., Pomykala, H., Yonebayashi, Y., Tanabe, S., Zeleznik-Le, N., and Rowley, J.D. (1996). Distribution of 11q23 breakpoints within the MLL breakpoint cluster region in de novo acute leukemia and in treatment-related acute myeloid leukemia: correlation with scaffold attachment regions and topoisomerase II consensus binding sites. Blood *87*, 1912–1922.

51. Xu, X., Wang, L., Hu, L., Dirks, W.G., Zhao, Y., Wei, Z., Chen, D., Li, Z., Wang, Z., Han, Y., et al. (2020). Small molecular modulators of JMJD1C preferentially inhibit growth of leukemia cells. Int. J. Cancer *146*, 400–412. https://doi.org/10.1002/ijc.32552.

52. Streubel, B., Valent, P., Jäger, U., Edelhäuser, M., Wandt, H., Wagner, T., Büchner, T., Lechner, K., and Fonatsch, C. (2000). Amplification of the MLL gene on double minutes, a homogeneously staining region, and ring chromosomes in five patients with acute myeloid leukemia or myelodysplastic syndrome. Genes Chromosomes Cancer *27*, 380–386.

53. Black, J.C., Van Rechem, C., and Whetstine, J.R. (2012). Histone lysine methylation dynamics: establishment, regulation, and biological impact. Mol. Cell *48*, 491–507. https://doi.org/10.1016/j.molcel.2012.11.006.

54. Liu, F., Barsyte-Lovejoy, D., Li, F., Xiong, Y., Korboukh, V., Huang, X.P., Allali-Hassani, A., Janzen, W.P., Roth, B.L., Frye, S.V., et al. (2013). Discovery of an in vivo chemical probe of the lysine methyltransferases G9a and GLP. J. Med. Chem. *56*, 8931–8942. https://doi.org/10.1021/jm401480r.

55. Atkin, N.D., Raimer, H.M., Wang, Z., Zang, C., and Wang, Y.H. (2021). Assessing acute myeloid leukemia susceptibility in rearrangement-driven patients by DNA breakage at topoisomerase II and CCCTC-binding factor/cohesin binding sites. Genes Chromosomes Cancer *60*, 808–821. https://doi.org/10.1002/gcc.22993.

56. Gothe, H.J., Bouwman, B.A.M., Gusmao, E.G., Piccinno, R., Petrosino, G., Sayols, S., Drechsel, O., Minneker, V., Josipovic, N., Mizi, A., et al. (2019). Spatial chromosome folding and active transcription drive DNA fragility and formation of oncogenic MLL translocations. Mol. Cell *75*, 267–283.e12. https://doi.org/10.1016/j.molcel.2019.05.015.

57. Phillips, J.E., and Corces, V.G. (2009). CTCF: master weaver of the genome. Cell *137*, 1194–1211. https://doi.org/10.1016/j.cell.2009.06.001.

58. Felix, C.A. (1998). Secondary leukemias induced by topoisomerase-targeted drugs. Biochim. Biophys. Acta *1400*, 233–255. https://doi.org/10.1016/s0167-4781(98)00139-0.

59. Sanjuan-Pla, A., Bueno, C., Prieto, C., Acha, P., Stam, R.W., Marschalek, R., and Menéndez, P. (2015). Revisiting the biology of infant t(4;11)/MLL-AF4+ B-cell acute lymphoblastic leukemia. Blood *126*, 2676–2685. https://doi.org/10.1182/blood-2015-09-667378.

60. Libura, J., Slater, D.J., Felix, C.A., and Richardson, C. (2005). Therapy-related acute myeloid leukemia-like MLL rearrangements are induced by etoposide in primary human CD34+ cells and remain stable after clonal expansion. Blood *105*, 2124–2131. https://doi.org/10.1182/blood-2004-07-2683.

61. Lehman, B.J., Lopez-Diaz, F.J., Santisakultarm, T.P., Fang, L., Shokhirev, M.N., Diffenderfer, K.E., Manor, U., and Emerson, B.M. (2021). Dynamic regulation of CTCF stability and sub-nuclear localization in response to stress. PLoS Genet. *17*, e1009277. https://doi.org/10.1371/journal.pgen.1009277.

62. Kumarapeli, A.R., Horak, K.M., Glasford, J.W., Li, J., Chen, Q., Liu, J., Zheng, H., and Wang, X. (2005). A novel transgenic mouse model reveals deregulation of the ubiquitin-proteasome system in the heart by doxorubicin. FASEB J. *19*, 2051–2053. https://doi.org/10.1096/fj.05-3973fje.

63. Mullighan, C.G. (2012). Molecular genetics of B-precursor acute lymphoblastic leukemia. J. Clin. Invest. *122*, 3407–3415. https://doi.org/10.1172/JCI61203.

64. Andersen, M.K., Autio, K., Barbany, G., Borgström, G., Cavelier, L., Golovleva, I., Heim, S., Heinonen, K., Hovland, R., Johannsson, J.H., et al. (2011). Paediatric B-cell precursor acute lymphoblastic leukaemia with t(1;19)(q23;p13): clinical and cytogenetic characteristics of 47 cases from the Nordic countries treated according to NOPHO protocols. Br. J. Haematol. *155*, 235–243. https://doi.org/10.1111/j.1365-2141.2011.08824.x.

65. Kager, L., Lion, T., Attarbaschi, A., Koenig, M., Strehl, S., Haas, O.A., Dworzak, M.N., Schrappe, M., Gadner, H., Mann, G., et al.; B.F.M.S.G. (2007). Incidence and outcome of TCF3-PBX1-positive acute lymphoblastic leukemia in Austrian children. Haematologica *92*, 1561–1564. https://doi.org/10.3324/haematol.11239.

66. Aplan, P.D. (2006). Chromosomal translocations involving the MLL gene: molecular mechanisms. DNA Repair (Amst) *5*, 1265–1272. https://doi.org/10.1016/j.dnarep.2006.05.034.

67. Gómez-Herreros, F., Zagnoli-Vieira, G., Ntai, I., Martínez-Macías, M.I., Anderson, R.M., Herrero-Ruíz, A., and Caldecott, K.W. (2017). TDP2 suppresses chromosomal translocations induced by DNA topoisomerase II during gene transcription. Nat. Commun. *8*, 233. https://doi.org/10.1038/s41467-017-00307-y.

68. Eisenmann, K.M., Dykema, K.J., Matheson, S.F., Kent, N.F., DeWard, A.D., West, R.A., Tibes, R., Furge, K.A., and Alberts, A.S. (2009). 5q- myelodysplastic syndromes: chromosome 5q genes direct a tumor-suppression network sensing actin dynamics. Oncogene *28*, 3429–3441. https://doi.org/10.1038/onc.2009.207.

69. Giagounidis, A.A., Germing, U., Wainscoat, J.S., Boultwood, J., and Aul, C. (2004). The 5Q- syndrome. Hematology *9*, 271–277. https://doi.org/10.1080/10245330410001723824.

70. Ebert, B.L., Pretz, J., Bosco, J., Chang, C.Y., Tamayo, P., Galili, N., Raza, A., Root, D.E., Attar, E., Ellis, S.R., and Golub, T.R. (2008). Identification of RPS14 as a 5Q- syndrome gene by RNA interference screen. Nature *451*, 335–339. https://doi.org/10.1038/nature06494.

71. Starczynowski, D.T., Kuchenbauer, F., Argiropoulos, B., Sung, S., Morin, R., Muranyi, A., Hirst, M., Hogge, D., Marra, M., Wells, R.A., et al. (2010). Identification of miR-145 and miR-146a as mediators of the 5Q- syndrome phenotype. Nat. Med. *16*, 49–58. https://doi.org/10.1038/nm.2054.

72. Aplan, P.D. (2006). Causes of oncogenic chromosomal translocation. Trends Genet. *22*, 46–55. https://doi.org/10.1016/j.tig.2005.10.002.

73. Hulegårdh, E., Nilsson, C., Lazarevic, V., Garelius, H., Antunovic, P., Rangert Derolf, Å., Möllgård, L., Uggla, B., Wennström, L., Wahlin, A., et al. (2015). Characterization and prognostic features of secondary acute myeloid leukemia in a population-based setting: a report from the Swedish Acute leukemia Registry. Am. J. Hematol. *90*, 208–214. https://doi.org/10.1002/ajh.23908.

74. Duy, C., Teater, M., Garrett-Bakelman, F.E., Lee, T.C., Meydan, C., Glass, J.L., Li, M., Hellmuth, J.C., Mohammad, H.P., Smitheman, K.N., et al. (2019). Rational targeting of cooperating layers of the epigenome yields enhanced therapeutic efficacy against AML. Cancer Discov. *9*, 872–889. https://doi.org/10.1158/2159-8290.CD-19-0106.

75. Li, H., and Durbin, R. (2010). Fast and accurate long-read alignment with Burrows-Wheeler transform. Bioinformatics *26*, 589–595. https://doi.org/10.1093/bioinformatics/btp698.

76. Ramírez, F., Ryan, D.P., Grüning, B., Bhardwaj, V., Kilpert, F., Richter, A.S., Heyne, S., Dündar, F., and Manke, T. (2016). deepTools2: a next generation web server for deep-sequencing data analysis. Nucleic Acids Res. *44*, W160–W165. https://doi.org/10.1093/nar/gkw257.

77. Heinz, S., Benner, C., Spann, N., Bertolino, E., Lin, Y.C., Laslo, P., Cheng, J.X., Murre, C., Singh, H., and Glass, C.K. (2010). Simple combinations of lineage-determining transcription factors prime cis-regulatory elements required for macrophage and B cell identities. Mol. Cell *38*, 576–589. https://doi.org/10.1016/j.molcel.2010.05.004.

78. Ross-Innes, C.S., Stark, R., Teschendorff, A.E., Holmes, K.A., Ali, H.R., Dunning, M.J., Brown, G.D., Gojis, O., Ellis, I.O., Green, A.R., et al. (2012). Differential oestrogen receptor binding is associated with clinical outcome in breast cancer. Nature *481*, 389–393. https://doi.org/10.1038/nature10730.

79. Van Rechem, C., Ji, F., Chakraborty, D., Black, J.C., Sadreyev, R.I., and Whetstine, J.R. (2021). Collective regulation of chromatin modifications predicts replication timing during cell cycle. Cell Rep. *37*, 109799. https://doi.org/10.1016/j.celrep.2021.109799.

80. Van Rechem, C., Ji, F., Mishra, S., Chakraborty, D., Murphy, S.E., Dillingham, M.E., Sadreyev, R.I., and Whetstine, J.R. (2020). The lysine demethylase KDM4A controls the cell-cycle expression of replicative canonical histone genes. Biochim. Biophys. Acta Gene Regul. Mech. *1863*, 194624. https://doi.org/10.1016/j.bbagrm.2020.194624.

STAR★METHODS

KEY RESOURCES TABLE

REAGENT or RESOURCE	SOURCE	IDENTIFIER
Antibodies		
Anti-KDM3B, clone C69G2	Cell Signaling	Cat# 3314; RRID: AB_1264294
Anti-JMJD1B	Invitrogen	Cat# PA5-53459
Anti-G9a	Sigma	Cat# G6919; RRID: AB_262007
Anti-beta Actin	Millipore	Cat# MAB1501; RRID: AB626633
Anti-Actinin	Santa Cruz	Cat# sc-17829; RRID: AB_626633
Goat anti-mouse HRP	Biorad	Cat# 170-6516; RRID: AB11125547
Goat anti-rabbit HRP	GenScript	Cat# A00167
Anti-H3K9me1	Abcam	Cat# ab8896; RRID:AB_732929
Anti-H3K9me2	Abcam	Cat# ab1220; RRID:AB_449854
Anti-H3K9me3	Abcam	Cat# ab8898; RRID:AB_306848
Anti-CTCF, clone D31H2	Cell Signaling	Cat# 3418; RRID:AB_2086791
Biological samples		
Primary AML	Cihangir Duy[74]	N/A
Chemicals, peptides, and recombinant proteins		
Pierce Protease Inhibitor Tablets	Thermo Scientific	Cat# A32953
Pierce Phosphatase Inhibitor Tablets	Thermo Scientific	Cat# A32957
Propidium Iodide Solution	Sigma Aldrich	Cat# P4864
Doxorubicin	Sigma Aldrich	ab142052
Doxorubicin (Mouse study)	Selleckchem	Cat# E2516
Dulbecco's Modified Eagles Medium – High Glucose	Sigma Aldrich	Cat# D5648
Roswell Park Memorial Institute Medium (RPMI)1640	Sigma Aldrich	Cat# R6504
Opti-Mem	Life Technologies	Cat# 31985070
Trypsin (0.25%) EDTA	Life Technologies	Cat# 2520056
L-Glutamine	Life Technologies	Cat# 25030-081
Penicillin and Streptomycin	Life Technologies	Cat# 15140122
Fetal Bovine Serum (FBS)	Gibco	Cat# 26140-079
Lipofectamine 3000	Life Technologies	Cat# L30000015
EHMTi	Jian Jin	UNC0642
KDM3i	Xu et al.[51]	JDI-12
Critical commercial assays		
miRNeasy Mini Kit	Qiagen	Cat# 217004
Superscript IV 1st Strand System	Life Technologies	Cat# 18091050
CL-XPosure™ Film	Thermo Scientific	Cat# 34091
Lumi-Light Western Blotting Substrate	Roche	Cat# 12015200001
Pierce BCA Protein Assay	Thermo Scientific	Cat# 23223 and 23224
Protein A Dynabeads	Thermo Scientific	Cat# 10002D
Protein G Dynabeads	Thermo Scientific	Cat# 10004D
TruSeq ChIP Sample Prep Kit Set A (48 samples)	Illumina	Cat# 10748010
NextSeq® 500/550 High Output Kit v2 (75 cycles)	Illumina	Cat# FC-404-2005
Bac-to-Bac™ Baculovirus Expression System	Thermo Scientific	Cat# 10359016
Dead Cell Apoptosis Kits with Annexin V	Life Technologies	Cat# V13241

(*Continued on next page*)

Continued

REAGENT or RESOURCE	SOURCE	IDENTIFIER
Deposited data		
Raw ChIP-sequencing	This paper	GEO: GSE210480
KDM3B ChIP-seq	Li et al.[41]	GEO: GSE71885
RPE CTCF ChIP-seq	ENCODE	GEO: GSM749673
GM12878 CTCF ChIP-seq	ENCODE	GEO: GSM733752
H1 CTCF ChIP-seq	ENCODE	GEO: GSM733672
bronchial_epithelial CTCF ChIP-seq	ENCODE	GEO: GSM749779
Bcell CTCF ChIP-seq	ENCODE	GEO: GSM1003474
HL-60 CTCF ChIP-seq	ENCODE	GEO: GSM749688
HCT116 CTCF ChIP-seq	ENCODE	GEO: GSM1022652
Experimental models: Cell lines		
RPE-hTERT1	Nick Dyson	N/A
U937	FCCC Cell Culture Facility	CRL-1593.2
HL60	ATCC	CCL-240
KG1a	ATCC	CCL-246.1
HSPC	Cihangir Duy[74]	N/A
Experimental models: Organisms/strains		
Mouse: C57BL/6 / 129/Sv	Jackson Labs	Strain# 101043
Oligonucleotides		
See Table S3 for oligonucleotides used	This paper	N/A
Recombinant DNA		
Halo-CTCF	Promega	Cat# FHC01807
Halo-KDM3B	Promega	Cat# FHC05559
Halo-Tag Alone	Promega	Cat# G6591
MLL-1 Probe	Oxford Gene Technology	Cat# LPH 506-A
MLL breakapart	Oxford Gene Technology	Cat# LPH 013-A
AML1 breakapart	Oxford Gene Technology	Cat# LPH 027-SA
BCL6 breakapart	Oxford Gene Technology	Cat# LPH 035-SA
EVL1 breakapart	Oxford Gene Technology	Cat# LPH 036-SA
TCRB breakapart	Oxford Gene Technology	Cat# LPH 048-SA
MLLT1	Oxford Gene Technology	Cat# LPH 508-A
MLLT3	Oxford Gene Technology	Cat# LPH 509-A
Chromosome 11 Alpha Satellite Red	Oxford Gene Technology	Cat# LPE 011R-A
E2A breakapart	Oxford Gene Technology	Cat# LPH 019-SA
5q del probe	Oxford Gene Technology	Cat# LPH 024
19p probe	Oxford Gene Technology	Cat# LPT19 PR-A
NMYC/LAF4 probe	Oxford Gene Technology	Cat# LPS-009A
MLL adjacent probe (*CD3*)	Empire Genomics	RPCI-11 215H18
Kmt2a/Chr9 Mouse	Empire Genomics	Mouse KMT2A-Chr09
Software and algorithms		
Scaffold 6.0	3i-intelligent imaging Innovations	https://www.intelligent-imaging.com/slidebook
BWA 0.7.13	Li and Durbin[75]	https://bio-bwa.sourceforge.net/bwa.shtml
DeepTools 2.4.3	Ramirez et al.[76]	https://deeptools.readthedocs.io/en/develop/content/installation.html
HOMER v4.10.3	Heinz et al.[77]	http://homer.ucsd.edu/homer/
DiffBind	Ross-Innes et al.[78]	https://bioconductor.org/packages/release/bioc/html/DiffBind.html

RESOURCE AVAILABILITY

Lead contact

Further information and requests for resources should be directed to and will be fulfilled by the lead contact, Johnathan Whetstine (johnathan.whetstine@fccc.edu).

Materials availability

This study did not generate new unique reagents.

Data and code availability

Data

Original ChIP-sequencing data has been deposited at GEO and are publicly available as of the date of publication. Accession numbers are listed in the key resources table. This paper analyzes existing, publicly available data. These accession numbers for the datasets are listed in the key resources table.

Code

No original code was used in this study.

Any additional information required to reanalyze the data reported in this paper is available from the lead contact upon request.

EXPERIMENTAL MODEL AND STUDY PARTICIPANT DETAILS

Cell Culture

Retinal pigment epithelial (RPE) cells were cultured in DMEM-high glucose (Sigma) media supplemented with 10% heat-inactivated fetal bovine serum (FBS), 100U/ml penicillin, 100μg/ml streptomycin, and 2mM L-glutamine. U937 cells were cultured in RPMI 1640 media supplemented with 10% heat-inactivated FBS, 100U/ml penicillin, 100μg/ml streptomycin and 2mM L-glutamine. HL60 and KG1a cells were cultured in RPMI 1640 media supplemented with 20% heat-inactivated FBS, 100U/ml penicillin, 100μg/ml streptomycin and 2mM L-glutamine. Cell line identities were authenticated by short tandem repeat analysis and Mycoplasma tested using the MycoAlert Detection Kit (Lonza, LT07-218). We are appreciative to the Cell Culture Facility at Fox Chase Cancer Center for their support.

Human primary patient-derived AML cases were obtained from Dr. Cihangir Duy's laboratory[74] and maintained in Iscove's modified Dulbecco's medium (IMDM; Thermo Fisher Scientific, Waltham, MA) containing 20% fetal bovine serum (Corning Premium FBS), 100 IU ml−1 penicillin, 100 μg ml−1 streptomycin, and 50 μM 2-mercaptoethanol. Cytokines, purchased from StemCell Technologies (Vancouver, BC, Canada), were added twice a week with SCF (50 ng ml−1), IL-3 (20 ng ml−1), IL-6 (20 ng ml−1), GM-CSF (20 ng ml−1), G-CSF (20 ng ml−1), and FLT-3 ligand (50 ng ml−1). For the AML organoid model, Human primary patient-derived AML cases were expanded using OP9 stroma feeder layers. OP9 feeder layers were generated using irradiation with 30 Gy before seeding the stroma cells on 0.01% poly-L-lysine-coated cell culture dishes to a confluency of 80-90%. The next day, patient-derived AML cells were seeded and maintained on the OP9 dishes in Iscove's modified Dulbecco's medium (IMDM; Thermo Fisher Scientific, Waltham, MA) containing 20% fetal bovine serum (Corning Premium FBS), 100 IU ml−1 penicillin, 100 μg ml−1 streptomycin, and 50 μM 2-mercaptoethanol. Cytokines were added twice a week with SCF (50 ng ml−1), IL-3 (20 ng ml−1), IL-6 (20 ng ml−1), GM-CSF (20 ng ml−1), G-CSF (20 ng ml−1), and FLT-3 ligand (50 ng ml−1). Expanding AML cells were transferred every 1–2 weeks after reaching a cell density of more than 1 million ml−1 onto fresh OP9 dishes supplemented with cytokines. For drug treatments, KDM3i (1μM) was supplemented directly to the media for 72 hrs.

Isolation of HSPCs

Mononuclear cells (MNC) were isolated from fresh human umbilical cord blood samples (New York Blood Center) using Ficoll (Atlanta Biologicals) density gradient centrifugation. These cells were obtained from Dr. Cihangir Duy's laboratory. After lysis of red blood cells, HSPCs were selected via immunomagnetic enrichment of $CD34^+$ MNCs using CD34 MicroBead Kit and Automacs from Miltenyi Biotech. HSPCs were maintained in Iscove's modified Dulbecco's medium (IMDM; Thermo Fisher Scientific, Waltham, MA) containing 20% fetal bovine serum (Corning Premium FBS), 100 IU ml−1 penicillin, 100 μg ml−1 streptomycin, and 50 μM 2-mercaptoethanol. OP9 feeder layers were generated using irradiation with 30 Gy before seeding the stroma cells on 0.01% poly-L-lysine-coated cell culture dishes to a confluency of 80-90%. The next day, HSPCs were seeded and maintained on the OP9 dishes in Iscove's modified Dulbecco's medium (IMDM; Thermo Fisher Scientific, Waltham, MA) containing 20% fetal bovine serum (Corning Premium FBS), 100 IU ml−1 penicillin, 100 μg ml−1 streptomycin, and 50 μM 2-mercaptoethanol. Cytokines were added twice a week with SCF (50 ng ml−1), IL-3 (20 ng ml−1), IL-6 (20 ng ml−1), GM-CSF (20 ng ml−1), G-CSF (20 ng ml−1), and FLT-3 ligand (50 ng ml−1). Cells were regularly selected for $CD34^+$ to maintain a pool of HSPCs. For drug treatments, KDM3i (1μM) was supplemented directly to the media for 72 hrs.

Mouse Model Details

The Institutional Animal Care and Use Committees review board at Temple University (approval number 5025) approved all mouse experiments. Mice used in this study were obtained from the Jackson Laboratory and maintained at Temple University in conventional housing with LabDiet 5053 irradiated food and Hydropacs filter sterilized water available ad libitum, on a 12L:12D light cycle, in 30-70% humidity with 10-15 air exchanges per hour. For the in vivo Doxorubicin treatment in Figure 6C, 3-5 months old mice of B6129SF1/J strain (The Jackson Laboratory 101043) were used. For the in vivo combination treatment in Figure 7E, 8-10 weeks old mice of B6129SF1/J strain (The Jackson Laboratory 101043) were used. Both male and female mice were tested in all conditions, and sex did not influence the results of the study.

METHOD DETAILS

Transfection Procedure for RPE cells

Cells were plated in 10 cm cell culture dishes and allowed to adhere for 16-20 hours. Cell culture medium was removed, cells were rinsed with phosphate buffered saline (PBS) and then replaced with OPTI-MEM medium (Life Technologies) prior to siRNA transfections (5nM-10nM/transfection). Transfections were changed to complete cell culture media after 4 hrs of transfection, and cells were collected 72 hrs post transfection. Transient overexpression transfections with 1-2μg of plasmid were performed using Lipofectamine 3000 transfection reagent and P3000 reagent (Life Technologies) in OPTI-MEM medium for 4 hrs, followed by changing to complete DMEM media for 24 hrs before collection. Silencer select negative controls and siRNAs were purchased from Life Technologies. Their sequences and unique identification numbers are tabulated in key resources table. For Figures 4A and S4A–S4G, cells were first transfected with siEHMT1/G9a siRNAs for 24 hrs followed by KDM3B siRNA transfection for 48hr. For co-transfection experiments (Figures 5B, 5J, S5A, S5B, S5H, and S5I), both the siRNAs were transfected at the same time and collected at 72 hrs from transfection.

Transfection procedure for U937, HL60 and KG1a cells

U937, KG1a and HL60 were transfected using Neon System (Invitrogen) following manufacturer's instructions. 500,000 cells were mixed with 10nM siRNA constructs in 10μl of supplied buffer. Cell mixture was loaded in Neon syringe and submerged in electrode buffer. For U937 cells, 3 pulses of 1400mV at 10ms was applied. For HL60 cells, 1 pulse of 1350 mV at 35ms was applied. For KG1a cells, 1 pulse of 1650mV at 20ms was applied. Cells were immediately transferred into fresh media in 6 well plates and allowed to grow for 72 hours.

Long-term passage of siRNA transfected cells

Control siRNA transfected and KDM3B siRNA transfected cells were considered as passage 0 (P=0) 72 hrs post transfection. After 72 hours post transfection, the $2.5X10^5$ cells were plated and cultured for 72 hrs as passage P=1. The cells were subsequently plated, passaged and harvested at indicated passage numbers. For example, passage 3 is ~9 days in culture and ~9 doublings for RPEs and ~6 doublings for U937 cells, respectively.

RNA extraction and quantitative real-time PCR

Cells were washed and collected by trypsinization after two PBS washes. Cell pellet was resuspended in Qiazol reagent (QIAGEN) for lysis and stored at -80°C before further processing. Total RNA was extracted using miRNAeasy Mini Kit (QIAGEN) with an on-column DNase digestion according to the manufacturer's instructions. RNA was quantified using NanoDrop 2000 or One (Thermo Scientific). Single strand cDNA was prepared using Super Script IV first strand synthesis kit (Invitrogen) using random hexamers. Expression levels were analyzed using FastStart Universal SYBR Green Master (ROX) (Roche) according to the manufacturer's instructions on a LightCycler 480 PCR machine (Roche) or QuantStudio 5 Real-time PCR machine (Applied Biosystems). Samples were normalized to β-actin. Primer sequences are provided in key resources table.

Immunoblotting

Cells were trypsinized and washed two times with PBS before resuspending in RIPA lysis buffer [50mM Tris pH 7.4, 150mM NaCl, 0.25% Sodium Deoxycholate, 1% NP40, 1mM EDTA, 10% Glycerol] freshly supplemented with Pierce Protease and Phosphatase inhibitor cocktails (ThermoFisher). Cells were lysed on ice for 15 min and stored at 80°C until further processing. Lysates were sonicated for 15 min (30sec ON and 30sec OFF cycle) at 70% amplitude in QSonica Q700 sonicator (Qsonica) followed by centrifugation at 12,000rpm for 15min. Cell lysate was transferred to a fresh tube and protein quantification was performed with Pierce BCA reagent (Thermo Scientific). Equal amounts of proteins were separated by SDS gel electrophoresis and transferred on nitrocellulose membrane (BioTrace NT, Pall Life Sciences) for at least 3 hrs at a constant current. The membranes were blocked for at least 1 hr in 5% BSA-PBST (1X PBS with 0.5% Tween-20) or 5% milk-PBST and probed over night with specific antibodies as follows at the following dilutions: anti-KDM3B (Cell Signaling) (1:1000); anti-β-Actin (Millipore) (1:10,000); anti-G9A (Sigma) (1:5000); anti-Actinin (Santacruz) (1:2000). Catalog numbers for all antibodies used in this study can be found in the key resources table. Membranes were washed three times in PBST the next day, incubated with goat anti-mouse IgG peroxidase conjugated secondary antibody (170-6516, Biorad) or goat anti-rabbit peroxidase conjugated secondary antibody (A00167, GenScript) at 1:2500 in 5% milk-PBST for at least 1hr at

room temperature, washed 3 times with PBST and incubated in Lumi-Light western blotting substrate (12015200001, Roche) 1min. Membranes were developed with CL-XPosure Films (34091, Thermo). The western blot images displayed in the figures have been cropped and auto-contrasted. Protein levels were quantified using ImageJ and normalized to the corresponding control protein levels.

Cell Cycle Analysis

Samples were washed with PBS, centrifuged at 1400rpm for 5 min, and permeabilized with 500mL PBS containing 0.5% Triton X-100 for 30 min. After this incubation, cells were washed with PBS and centrifuged at 1400rpm for 5 min. Samples were then stained with 1:100 dilutions of 1mg/mL PI solution and 0.5M EDTA with 100 mg RNase A, overnight at 4°C. Cell cycle distribution was analyzed by flow cytometry using the LSRII flow cytometry system (BD Biosciences). We are grateful to the Cell Sorting Facility at Fox Chase Cancer Center for assistance with flow cytometry.

DNA Fluorescent *In Situ* Hybridization (FISH)

The FISH protocol was performed as described previously in.[7] Briefly, cell suspensions were fixed in ice-cold methanol:glacial acetic acid (3:1) solution for a minimum of four hours, before being centrifuged onto 8 Chamber Polystyrene vessel tissue culture treated glass slides (Falcon, Fisher Scientific) at 900rpm. The slides were air-dried and incubated in 2X SSC buffer for 2 min, followed by serial ethanol dilution (70%, 85% and 100%) incubations for 2 min each, for a total of 6 min. Air-dried slides were hybridized with probes that were diluted in appropriate buffer overnight at 37°C. The slides were washed the next day for 3 to 4 mins in appropriate wash buffers at 69°C with 0.4X SSC for Cytocell probes, Agilent Buffer1 for Agilent probes, or 0.4X SSC + 0.3% NP-40 for Empire Genomic probes followed by washing in 2X SSC with 0.05% Tween-20 (Cytocell probes), Agilent Buffer 2 (Agilent) or 2X SSC+0.1% NP-40 (Empire). The slides were incubated in 1mg/mL DAPI solution made in 1% BSA-PBS, followed by a final 1X PBS wash. After the wash, the slides were mounted with ProLong Gold antifade reagent (Invitrogen).

FISH images were acquired using an Olympus IX81 or Olympus IX83 spinning disk microscope at 40X magnification and analyzed using Slidebook 6.0 software. A minimum of 20 z-planes with 0.5μm step size was acquired for each field. Copy number gains for MLL1,11C, NMYC/LAF4 were scored in RPE cells as three or more foci. For MLL break apart probe, copy gains were scored as 3 or more foci for the N terminus flanking probe (green) and C terminus flanking probe (red). Complete separation of red and green probe with no overlap was called break apart for the MLL locus, TCF3 locus and any other locus FISHed with dual break apart probe. A minimum of 200 nuclei are scored for each independent experiment unless otherwise specified. Extended list of probes used are provided in the key resources table.

Metaphase Spreads

RPE cells were transfected with siRNAs and passed 3 times. Cells were seeded for 48 hours. The cells were treated with KaryoMAX colcemid solution (Gibco) at a final concentration of 2μg/mL for 3 hrs and were collected by mitotic shake off, washed with 1X PBS followed by 0.59% KCl (w/v) hypotonic solution for 40 mins for expansion and swelling. The reaction was terminated by addition of 3:1 solution of cold methanol:acetic acid, followed by 4 washes. The cells were then resuspended in fixative solution. The cells were pipetted and dropped on a glass slide from a height of 12–15 inches to make the metaphase spread. FISH was performed for the indicated probes post drying of the slides. The images were taken with 30 z-planes with 0.5 μm step size using the Olympus IX83 microscope. The images were analyzed using Slidebook 6.0 software.

Protein purification

Human full length of KDM3A, KDM3B and KDM5A were cloned into pFastbac1 with flag tag at N-terminal, then bacmid were made to produce baculovirus in insect cells (sf9) using the Bac-to-Bac™ Baculovirus Expression System (Thermo Scientific). Cells were harvested 42 hours after baculovirus infection by centrifugation (2000rpm, 4 degree), then the pellet was lysed in lysis buffer (Tris-HCL(PH7.5) 25mM, NaCl 300mM, Triton 0.1%, PMSF 1mM, DTT 1mM) by sonication and centrifuged at 14000rpm for 30 minutes. The supernatant was incubated with Flag-M2 agarose beads for 5 hours, unbound proteins were removed by washing the beads with lysis buffer 4 times, and the proteins enriched were eluted with 3Xflag peptide (0.15mg/ml) diluted in elution buffer (Tris-HCL(PH7.5) 25mM, NaCl 150mM, DTT 1mM). Proteins purified were used for SDS-PAGE and biochemical reaction analysis. Coomassie staining of KDM3B and KDM5A in Figure S1D was spliced to place the KDM3B and KDM5A lanes next to the ladder due to other purified proteins being placed between them.

Histone demethylase reactions

400ng KDM3A, KDM3B and KDM5A were incubated with 1μg bulk histones (Histone from calf thymus) or 3.3μM H3K9me2 peptide in 30μl reaction system at 27 C for 5 hours. Reaction buffer: Hepes(PH7.5) 50mM, 2-OG 50μM, Fe(NH4)2(SO4)2 50μM, Sodium L-Acorbate 400μM, TCEP 1mM.

Recombinant human KDM3B/JMJD1B protein (abcam ab271569) was incubated with 1μM KDM3i, 1M Tris, 5M NaCl, 10mM Asorbic Acid, 10mM α-Ketoglutarate, 10mM Fe(NH4)2(SO4)2(H2O)6 at 27 C, 30 minutes. 1μL Histone from Calf Thymus (1mg/mL) in H2O was added to make reaction 100μL then incubated at 27 C for 5 hrs. 4X Laemmli Loading buffer with 5% β-Mercaptoethanol was added to reaction and then heated 95 C for 10 mins. Samples were snap frozen and then used for western blots.

Digital Droplet PCR

The Digital Droplet PCR (ddPCR) was performed using 10 μL of 2 × ddPCR Supermix for Probes (no dUTP) (Bio-Rad), 900 nM of each primer, 250 nM probe, 50 ng of digested DNA template using HindIII restriction enzyme (NEB) and r2.1 Buffer (NEB), and nuclease free water to a total volume of 20 μL. The QX200 droplet generator (Bio-Rad) was used to generate the droplet mixture. The droplet mixture was then transferred to a PCR reaction plate and amplified with the following conditions: denaturation of 95 °C for 10 min, followed by 40 cycles of a two-step thermal profile consisting of 95 °C for 15 s and 60 °C for 60 s, then incubated at 98 °C for 10 min and cooled to 8°C until the droplets were read. Once complete, the plate was transferred to the QX200 droplet reader (Bio-Rad) and analyzed for copy number variation (CNV). The number of positive (high level of fluorescence) and negative (low and constant level of fluorescence) droplets obtained were analyzed using QuantaSoft software (Bio-Rad, Pleasanton, CA, USA). Ratios of *KMT2A* to *CD3E* gene were used to determine copy number. Primer and probe sequences are provided in key resources table.

Drug Treatment Conditions

For Doxorubicin treatment, RPE cells were plated in 10 cm tissue culture plates at a density of $2.5x10^5$. Cells were allowed to adhere for approximately 16 hrs before Doxorubicin (Sigma) (dissolved in DMSO) was supplemented to media in different concentrations. Final concentrations used were 5, 2.5 and 1pg/μl. Cells were cultured in Doxorubicin for a total of 72 hrs before harvesting. For Figures 7B, 7F, S7C, and S7G cells were transfected with KDM3B or CTCF plasmid for 4 hrs. After removal of transfection mixture, cells were supplemented with 1 pg/μl Doxorubicin supplemented media and cultured for 20 hours before harvesting. For Figures 7C, S7D, and S7E, Doxorubicin was supplemented to the media 48hrs post G9a transfection and 24 hrs before harvesting. For Figures 6J and S6D–S6F, KG1a cells were cultured at a density of $2.5x10^5$/ml before Doxorubicin was added at a concentration of 60pg/μl for a total of 72 hrs before harvesting.

For JDI12 (KDM3i) treatment, KDM3i[51] was synthesized for these studies. $3x10^5$ RPE cells were plated in 10cm tissue culture plates. Cells were allowed to adhere to the plate for a minimum of 24 hrs before KDM3i (dissolved in DMSO) was supplemented to media at 25nM unless specified differently. For cancer and primary cell lines in Figures 2B–2E, cells were treated with 1μM KDM3i. Cells were cultured for a total of 72 hrs before harvesting. For washout experiment (Figure 2F), cells were allowed to adhere 24 hrs before treatment with JDI12/KDM3i. Cells were treated for 12 hrs before media was removed, plates were washed with 1X PBS, and cells were either harvested or fresh complete media was added back to the plate without KDM3i. For passage experiments, RPE cells were plated at $1.5x10^5$ cells. Cells were allowed to adhere to the plate for 24 hrs before KDM3i was supplemented to media at 25nM. Cells were cultured in KDM3i for 72 hrs further before being harvested and passaged at $3x10^5$ per 10cm plate. Cells were passaged every 3 days and seeded at the same amount each passage.

For KG1a, Primary AML, AML Organoid, and HSPC KDM3i treatments in Figure 2, media was supplemented with 1μM KDM3i for 72 hrs before harvesting as described in the DNA FISH methods section.

For KDM3i + EHMTi (UNC0642) experiments, cells were seeded at $3x10^5$ in 10cm tissue culture plates and allowed to adhere for 60 hrs before media was supplemented with KDM3i (25nM) and EHMTi (2.5μM). Cells were harvested 12 hrs post treatment. For siCTCF + EHMTi experiments, cells were seeded in 10cm tissue culture plates at $2.1x10^5$ and allowed to adhere for 24 hrs before following the transfection procedure described above. 24 hrs post-transfection, media was supplemented with 1.5 μM EHMTi. Cells were cultured for a further 48 hrs (72 hrs total transfection) before being harvested. For Dox+EHMTi experiments, cells were plated at $1.5x10^5$ and allowed to adhere for 24 hrs. EHMTi was supplemented to media at a final concentration of 1.5μM. 48 hrs later Dox was supplemented to the media at 1pg/μl. 24 hrs after Dox supplement (72 hrs total EHMTi, 24 hrs total Dox), cells were harvested.

For MG132 treatment, cells were seeded at $1.5x10^5$ in 10cm tissue culture plates and allowed to adhere for 24hrs before media was supplemented with 5pg/μL of Dox. 48hrs later, 10μM MG132 was supplemented to the media. 24hrs after MG132 addition, plates were placed on ice, media was collected and cells were scraped into media before being washed twice in PBS and resuspended in RIPA lysis buffer.

Chromatin Immunoprecipitation

Chromatin was prepared and ChIP were performed as described in Van Rechem et al.[79] Specifically, sonication of chromatin was done with the Qsonica Q800R2 system (Qsonica). RPE cells were seeded in 10cm plates. At ~80% confluence, crosslinking of the cells was done by adding 1% formaldehyde to the media for 13 min at 37°C and stopped with 0.125M glycine, pH2.5. Plates were washed with ice cold PBS and scraped off, followed by centrifugation at 800 rpm for 2 min at 4°C. The pellet was resuspended in cellular lysis buffer (5mM PIPES pH8.00, 85mM KCl, 0.5% NP40) supplemented with protease inhibitors, incubated 5 min on ice and centrifuged at 800 rpm, 2 min at 4°C. The pellet was resuspended in nuclear lysis buffer supplemented with protease inhibitors (NLB, 50mM Tris, pH 8.0, 1.0% SDS, or 0.2% SDS for CTCF ChIP).

Chromatin was sonicated at 70% amplitude 15sec on 45sec off setting for 35 min or 45 min for CTCF ChIP. 5 μL of chromatin was RNase treated, and reverse cross-linked at least 4 hrs at 65°C in presence of proteinase K. DNA was isolated by phenol:chloroform extraction and checked on 1.3% agarose gel for a smear below 300bp. Chromatin was precleared by centrifugation at 14,000rpm for 10min at 4°C. Chromatin concentration was then quantified on a NanoDrop One. For each IP, 1-10μg of chromatin was immunoprecipitated with 0.2-2μg of antibody in dilution IP buffer (16.7mM Tris pH 8.0, 1.2mM EDTA pH 8.0, 167mM NaCl, 0.2% or 0.1% SDS, 0.24% Triton-X-100 or 1.84% for CTCF ChIP) at 4°C overnight. % SDS for dilution IP depended on % SDS used in Nuclear Lysis Buffer. Final concentration for IP was always 0.2% SDS. Chromatin was precleared for 2 hrs each with protein A agarose and

magnetic protein A or protein G beads (Invitrogen; to match antibody isotype) rotating at 4°C before immunoprecipitation. The immunoprecipitated material was washed 2 times in dilution IP buffer, 1 time in TSE buffer (20mM Tris pH 8.0, 2mM EDTA pH8.0, 500mM NaCl, 1% Triton X-100, 0.1% SDS), 1 time in LiCl buffer (100mM Tris pH 8.0, 500mM LiCl, 1% deoxycholic acid, 1% NP40) and 2 times in TE (10mM Tris pH 8.0, 1mM EDTA pH 8.0) before elution in elution buffer (50mM NaHCO3, 140mM NaCl, 1% SDS) with RNase treatment, followed by 10μg proteinase K at 1 hr 55°C 1000 rpm. The samples were removed from beads and reverse cross-linked at 65°C for 4 hrs. Immunoprecipitated DNA was purified using either PCR purification columns (Promega) or AMPureXP beads. All the ChIPs were performed with at least two independent chromatin preparations from two independent siRNAs or two independent RPE cell lines. Antibodies used for ChIP are as follows: H3K9me1 Abcam ab8896-100, H3K9me2 Abcam ab1220, H3K9me3 Abcam ab8898, CTCF (D31H2) Cell Signaling #3418. ChIP sequencing libraries were prepped using the TruSeq ChIP Sample Preparation kit (Illumina). Libraries were single-end sequenced (75 cycles) using a NextSeq500 (Illumina). ChIP-qPCR in Figures 5E and 7A was performed with 1μl of ChIP DNA with the following primers: **(*KMT2A Ex11*)** Forward - 5'-TCTGTCACGTTTGTGGAAG-3', Reverse - 5'-GCCCAGCTGTAGTTCTATTAC-3'. **(CTCF *negative site*)** Forward - 5'-GAATCAGACTGAGACCCTAAAC-3', Reverse 5'-GCCAATCCAGTCTTCTCATAC-3'. ChIP-qPCR in Figure S7B was performed with 1μl of ChIP DNA with the following primers: **(*KMT2A* CTCF flanking site)** Forward - 5'-CAGCCAGAATCCCAGTAGA-3', Reverse 5'-CTTTCAGAGGAGGCTACAGA-3'.

In vivo Doxorubicin

For the *in vivo* Doxorubicin treatment in Figure 6C, 3-5 months old mice of the mixed background (C57BL/6 and 129/Sv) 4 males and 4 females were used. The mice were randomly assigned to two groups – Dox (treated with 1.5mg/kg doxorubicin (Selleckchem) at the total volume of 100μl administered via i.v.) and control (treated with 100μl saline i.v. for 3 days). 24hrs after the last dose was administered the mice were euthanized. The spleen was isolated, any connective tissue was trimmed, and the organ was passed through 70μm cell strainer to receive suspension of single cells. Red blood cells were lysed using ACK buffer (Gibco) for 5 min on ice, then washed twice with PBS. Cells were then fixed for DNA FISH as described above.

For the *in vivo* combination treatment in Figure 7E, Doxorubicin (Selleckchem) was solubilized in saline and EHMTi was first solubilized in DMSO to 100 mg/ml and then a stock solution was prepared in saline. 7 male and 8 female mice of B6129SF1/J strain (The Jackson Laboratory 101043) were assigned into 4 groups treated with: i) vehicle (n=4, two males, two females); ii) 4 doses of EHMTi (daily, i.p. 5mg/kg) (n=4, two males, two females); iii) 3 doses of Doxorubicin (daily i.v. 1.5 mg/kg) (n=4, two males, two females); iv) 4 doses of EHMTi with 3 doses of Doxorubicin implemented into the treatment starting day 2 (n=3, one male, two females). The day after the final treatment, mice were euthanized, and the cells were isolated from spleen for double blinded examination by *Kmt2a* and control FISH (*Control 9*).

Annexin V Staining

$3x10^5$ control or *KMT2A* inherited cells were seeded in a 10 cm plate and grown asynchronously for 72 hours. Cells were treated with 25nM of KDM3i for 12, 6, or 3 hours before prior to harvesting. Collected cells were processed using ALEXA FLUOR 488 conjugated Annexin V and PI staining following the manufacturer's instructions (Life Technologies). Briefly, 1X annexin-binding buffer and 100 μg/mL PI solution were prepared. Harvested cells were washed once with 1X PBS before being resuspended in 1X annexin-binding buffer at a density of $1x10^6$ cells/mL in 100 μL. 5 μL of FITC Annexin V and 1 μL of the 100 μg/mL PI solution were added to each 100 μL cell suspension. Cells were incubated at room temperature for 15 minutes and then 400 μL of 1X annexin-binding buffer was added to each sample. Stained cells were analyzed by flow cytometry, measuring fluorescence at 530 nm and 600 nm. Data was collected on a BD Biosciences Symphony A5 flow cytometer and analyzed using FACSDiva software.

QUANTIFICATION AND STATISTICAL ANALYSIS

DNA FISH quantification

All pairwise comparisons were done using two-tailed Student's t-test unless otherwise stated. Significance was determined if the p value was ≤ 0.05. All FISH experiments were carried out with at least two independent siRNAs and at least 200 nuclei per replicate were counted for all the FISH studies conducted unless otherwise stated. All FISH studies had a minimum of 2 replicates, and therefore at least 400 nuclei were scored for each panel unless otherwise stated. All error bars represent the SEM.

ChIP-seq analysis

ChIP-seq analysis was performed as previously described.[9,79,80] Sequencing reads were aligned against the human hg19 reference genome using BWA.[75] Alignments were filtered for uniquely mapped reads and duplicates were removed. Input-normalized ratio coverage tracks were generated using Deeptools.[76] Peaks were called using HOMER[77] with default parameters.

For genome-wide analyses of H3K9me1 and H3K9me2 densities, we calculated input-normalized densities at all 10 Kb bins across the genome using bamcompare function of DeepTools. For genome-wide analysis of CTCF peaks, we mapped CTCF ChIP-seq reads using BWA and normalized ChIP read density by input using bamcompare function of DeepTools. Peaks were called using the Homer package.[77] Differential peaks between control and KDM3B knockdown were identified using DiffBind package,[78] with cutoffs of >2-fold change in KDM3B knockdown compared to control. We used the resulting ~17000 decreasing CTCF peaks to compare the ChIP-seq density of H3K9me1 and H3K9me2 between control and KDM3B knockdown cells at two types of regions,

the vicinity of each CTCF peak (10 Kb region of ± 5 Kb from the peak center) and two flanking 10 Kb regions to the left and right of this central region.

Genome-Wide analysis of CTCF peaks

CTCF ChIP-seq reads were mapped using BWA and normalized ChIP read density by input using bamcompare function of DeepTools. Peaks were called using the Homer package.[77] Differential peaks between control and KDM3B knockdown were identified using DiffBind package,[78] with additional cutoffs of >2-fold change and P-value < 0.05. The resulting set of differential peaks was used to compare the ChIP-seq density of H3K9me1 and H3K9me2 between control and KDM3B knockdown cells at the vicinity of each CTCF peak (10 Kb region of ± 5 Kb from the peak center).

Supplemental figures

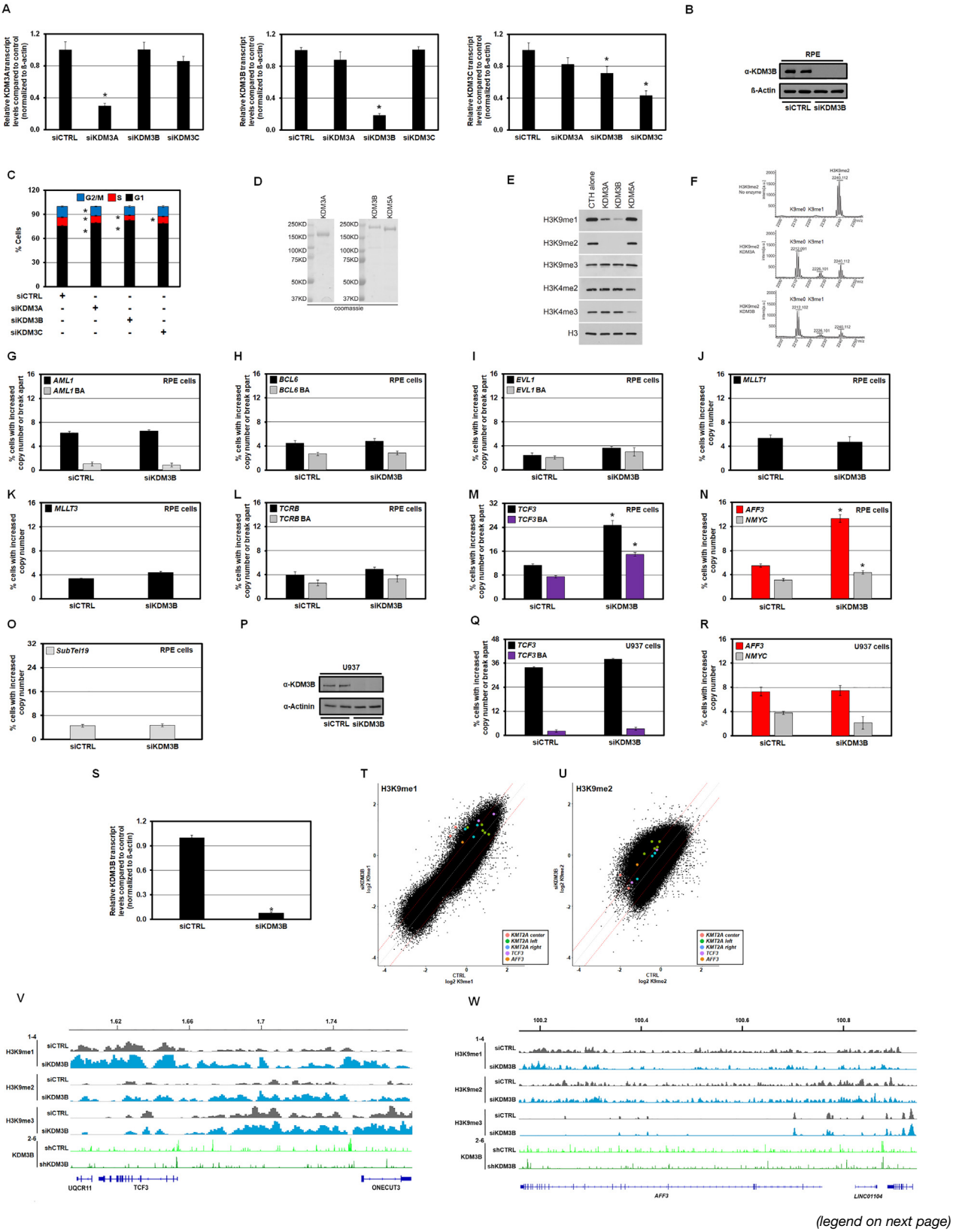

(legend on next page)

Figure S1. KDM3B depletion induces *KMT2A* DNA copy gains and break aparts, related to Figure 1

(A) RT-qPCR analysis was performed to validate specific gene siRNA knockdowns for the KDM3 family. Samples were normalized to β-actin.

(B) Western blot demonstrates that KDM3B protein levels are reduced when compared with controls using two different siRNAs in RPE cells.

(C) Fluorescence-activated cell sorting (FACS) analysis was performed after KDM3 family member siRNA depletion after 72 h.

(D) Coomassie gel of purified KDM enzymes used in the demethylase assay.

(E) Western blot of histones after being incubated with purified KDM3A,B and KDM5A. CTH alone- calf thymus histones alone.

(F) MALDI-TOF analyses of H3K9me2 peptides incubated with KDM3A or KDM3B.

(G–N) DNA FISH for various genomic regions tested upon KDM3B siRNA depletion. Only *TCF3/E2A* (M) and *AFF3/LAF4* (N) have significant copy gains and break aparts, or copy gains, respectively, upon KDM3B depletion in RPE cells when compared with the other loci tested.

(O) DNA FISH quantification for S*ubtel19* (appropriate control for M) that does not change upon KDM3B siRNA depletion.

(P) Western blot shows decreased KDM3B protein levels in U937 cells upon siKDM3B.

(Q) DNA FISH quantification for *TCF3/E2A* demonstrates no significant copy gains or break aparts in KDM3B siRNA-depleted U937 cells.

(R) DNA FISH quantification for *AFF3/LAF4* demonstrates no significant copy gains in KDM3B siRNA-depleted U937 cells.

(S) qPCR validation shows decreased KDM3B transcript levels compared with control in KDM3B siRNA-depleted cells. These cells were used for experiments represented in (T)–(V) and Figures 1L and 1M.

(T) Genome-wide effects of siKDM3B on H3K9me1 levels. Scatterplots show all 10 kb bins across the genome, with input-normalized H3K9me1 ChIP-seq densities in two conditions at each bin represented as a point. Red points, 10 kb bins overlapping the central region of KMT2A gene (containing exons 8–14: chr11 bins 118.35–118.36 and 118.36–118.37 Mbp). Green points, 10 kb bins overlapping the 5′ region of *KMT2A* (exons 1–8: chr11 bins 118.30–118.31, 118.31–118.32, 118.32–118.33, 118.33–118.34, and 118.34–118.35 Mbp). Blue points, 10 kb bins overlapping the 3′ region of *KMT2A* (exons 14–36: chr11 bins 118.37–118.38, 118.38–118.39, and 118.39–118.40 Mbp). Purple points, 10 kb bins overlapping with *TCF3* (chr11 bins 1.61–1.62, 1.62–1.63 Mbp). Orange point, 10 kb bin overlapping with *AFF3* (chr2 bin 100.17–100.18 Mbp). Genomic positions are based on GRCh37/hg19.

(U) Genome-wide effects of siKDM3B on H3K9me2 levels. Scatterplots show all 10 kb bins across the genome, with input-normalized H3K9me2 ChIP-seq densities in two conditions at each bin represented as a point. Colored points correspond to the bins listed in (T). Red points, 10 kb bins overlapping the central region of KMT2A gene (containing exons 8–14). Green points, 10 kb bins overlapping the 5′ region of KMT2A (exons 1–8). Blue points, 10 kb bins overlapping the 3′ region of KMT2A (exons 14–36). Purple points, 10 kb bins overlapping with *TCF3*. Orange point, 10 kb bin overlapping with *AFF3*. Genomic positions are based on GRCh37/hg19.

(V) Genomic tracks of input-normalized ChIP-seq densities of H3K9me1–3 and the public input-normalized KDM3B ChIP-seq density[41] for the region flanking *TCF3/E2A* upon depletion of KDM3B.

(W) Genomic tracks of input-normalized ChIP-seq densities of H3K9me1–3 and the public input-normalized KDM3B ChIP-seq density[41] for the *AFF3* region upon depletion of KDM3B.

Error bars represent the SEM. Asterisk indicates significant difference from indicated ($p < 0.05$) by two-tailed Student's t test. A minimum of 2 replicates per experiment were conducted. For FISH, a minimum of 100 nuclei were scored per replicate per experiment. BA, break aparts.

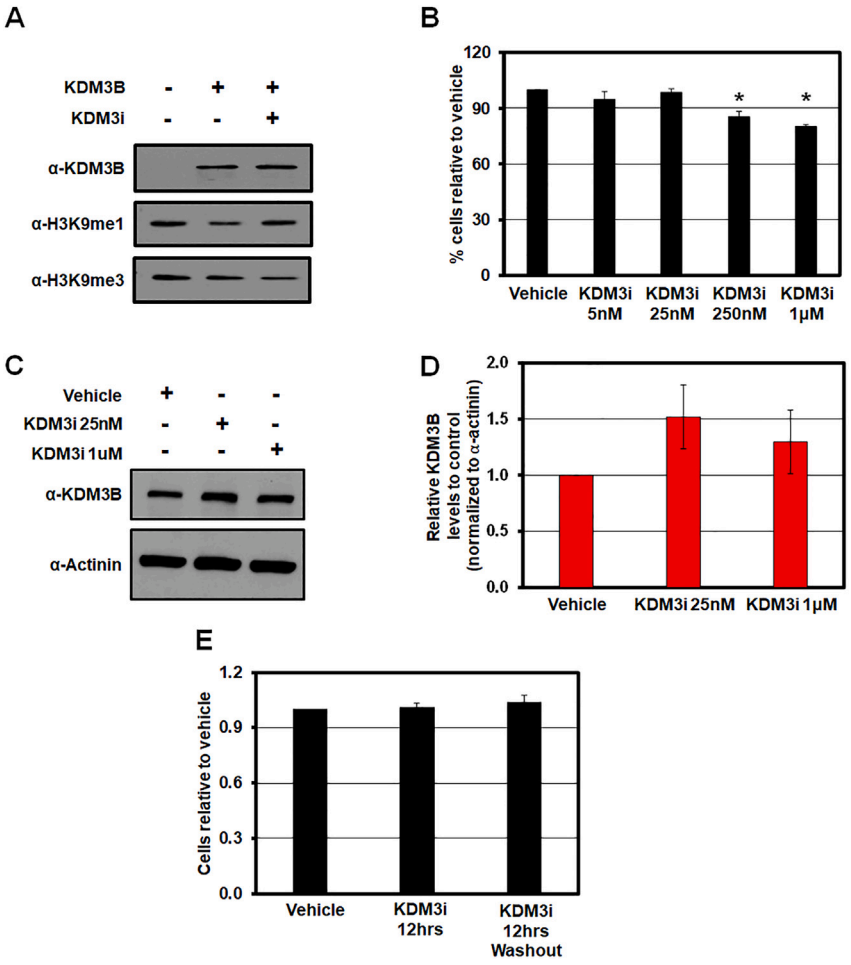

Figure S2. KDM3B chemical inhibition (KDM3i) promotes transient *KMT2A* copy gains and break aparts, related to Figure 2

(A) *In vitro* KDM assay with commercial full-length purified KDM3B protein incubated with histones and western blotted for KDM3B, H3K9me1, and H3K9me3. Blot demonstrates reduction in H3K9me1 levels upon incubation with KDM3B, which is rescued with KDM3i addition.

(B) Cell growth assay for KDM3i-treated RPE cells. Treatment with KDM3i at 25 nM does not impact cell growth, whereas that at 250 nM and 1 μM modestly but significantly suppresses growth.

(C) Western blot demonstrating KDM3B protein levels are not reduced with KDM3i treatment in RPE cells. A representative example from quantification in (D).

(D) Quantification of western blots for KDM3B in KDM3i-treated RPE cells (n = 3). KDM3B levels are not reduced upon treatment with KDM3i.

(E) Cell growth assay for KDM3i-treated RPE cells corresponding to Figure 2F. Cell growth is not impacted after 12 h KDM3i treatment, or after 12 h of KDM3i washout.

Error bars represent the SEM. Asterisk indicates significant difference from indicated ($p < 0.05$) by two-tailed Student's t test. A minimum of 2 replicates per experiment were conducted.

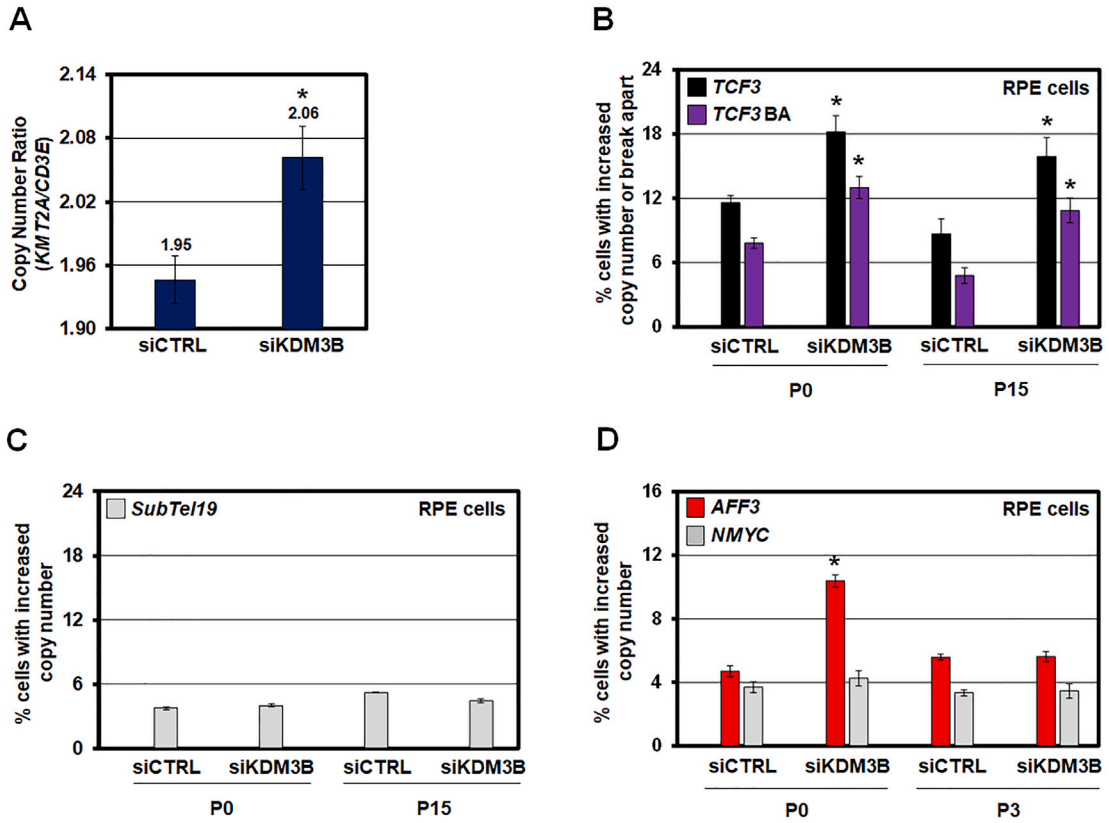

Figure S3. KDM3B suppression leads to integration and inheritance of *KMT2A* copy gains and break aparts, related to Figure 3

(A) Copy number variation analysis using digital droplet PCR (ddPCR) shows *KMT2A* copy number increase in later passage of the inherited *KMT2A* cell lines used in Figures 3G and 3H. Copy number is quantified by computing ratio of *KMT2A* to *CD3E* reference gene (4 biological replicates with 2 technical replicates).

(B) Quantification of DNA FISH for *TCF3/E2A* after passaging KDM3B siRNA-depleted RPE cells. *TCF3/E2A* copy gain and break aparts are retained after 15 passages in KDM3B siRNA-depleted cells.

(C) DNA FISH for *SubTel19* after passaging KDM3B siRNA-depleted RPE cells. *Subtel19* copy gain does not change in KDM3B siRNA-depleted cells.

(D) DNA FISH for *AFF3/LAF4* after passage of KDM3B siRNA-depleted RPE cells. *AFF3* copy gains occur at P0 but are not retained after 3 passages in KDM3B siRNA-depleted cells. *NMYC* copy gain does not change.

Error bars represent the SEM. Asterisk indicates significant difference from indicated ($p < 0.05$) by two-tailed Student's t test. A minimum of 2 replicates per experiment were conducted. For FISH, a minimum of 200 nuclei were scored per replicate per experiment. BA, break aparts.

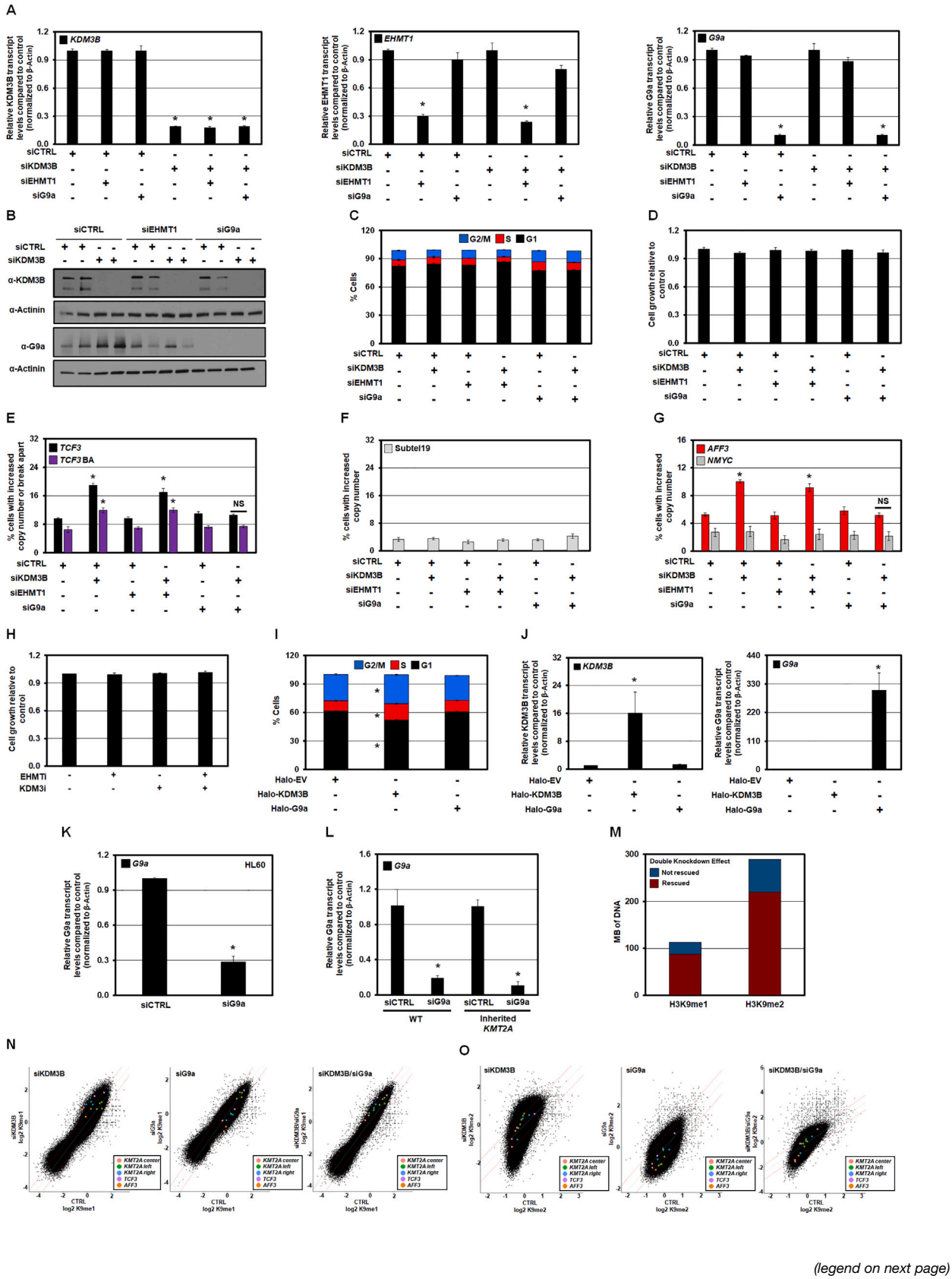

(legend on next page)

Figure S4. H3K9me1 balance controls *KMT2A* copy gains and break aparts, related to Figure 4

(A) RT-qPCR analysis was performed to validate gene-specific siRNA knockdowns. Samples were normalized to β-actin.

(B) Western blot images demonstrating successful siRNA-mediated depletion of KDM3B and G9a protein in RPE cells.

(C) FACS analysis evaluating cell cycle dynamics was performed for the siRNA-mediated co-depletion experiments.

(D) Cell growth assays for siRNA co-depletion of KDM3B, EHMT1, and/or G9a.

(E) DNA FISH quantification for siRNA co-depletion of KDM3B, EHMT1, and/or G9a. siRNA-depleted G9a but not EHMT1 prevents *TCF3*/*E2A* copy gains and break aparts upon KDM3B depletion in RPE cells.

(F) DNA FISH quantification of SubTel19 (control for *TCF3* region) for siRNA co-depletion of KDM3B, EHMT1, and/or G9a.

(G) DNA FISH quantification for siRNA co-depletion of KDM3B, EHMT1, and/or G9a. siRNA-depleted G9a but not EHMT1 prevents *AFF3*/*LAF4* copy gains upon KDM3B depletion.

(H) Cell growth assays for KDM3/EHMT inhibitor vs. control treatments corresponding to Figure 4B.

(I) FACS analysis evaluating cell cycle dynamics was performed for cells with KDM3B and/or G9a overexpression.

(J) RT-qPCR analysis for KDM3B and G9a overexpression in RPE cells. Samples were normalized to β-actin.

(K) RT-qPCR analysis was performed to validate gene-specific siRNA knockdowns in HL60 cells. Samples were normalized to β-actin.

(L) RT-qPCR analysis was performed to validate gene-specific siRNA knockdowns in WT vs. inherited *KMT2A* cells. Samples were normalized to β-actin. Two independent stable cell lines were used per condition with two independent siRNAs.

(M) Across the genome, the increase of H3K9me1 and H3K9me2 caused by siKDM3B was mostly rescued by double KDM3B and G9a knockdown. Barplots showing the fractions of the genome (based on 10 kb genomic bins) that increased H3K9me1 (left) and H3K9me2 (right) upon KDM3B knockdown. Red, genomic fraction, where this increase was rescued by double knockdown.

(N) Genome-wide effects of siKDM3B, siG9a, and double knockdown on H3K9me1 levels. Scatterplots show all 10 kb bins across the genome, with input-normalized H3K9me1 ChIP-seq densities in two conditions at each bin represented as a point. KDM3B and G9a knockdowns have opposite skews, whereas the double knockdown strongly reduces these H3K9me1 changes. Left, scatterplot comparing H3K9me1 densities in control vs. siKDM3B; H3K9me1 changes are skewed toward increase (points above the upper red line correspond to >1.5-fold increase in siKM3B cells). Middle, scatterplot for control vs. siG9a cells; H3K9me1 changes are skewed toward decrease (points below the lower red line correspond to >1.5-fold decrease in siG9a cells). Right, scatterplot for control vs. siKDM3B + siG9a cells, with much fewer H3K9me1 changes in either direction. Red points, 10 kb bins overlapping the central region of KMT2A gene (containing exons 8–14: chr11 bins 118.35–118.36 and 118.36–118.37 Mbp). Green points, 10 kb bins overlapping the 5′ region of KMT2A (exons 1–8: chr11 bins 118.30–118.31, 118.31–118.32, 118.32–118.33, 118.33–118.34, and 118.34–118.35 Mbp). Blue points, 10 kb bins overlapping the 3′ region of KMT2A (exons 14–36: chr11 bins 118.37–118.38, 118.38–118.39, and 118.39–118.40 Mbp). Purple points, 10 kb bins overlapping with *TCF3* (chr19 bins 1.61–1.62, 1.62–1.63 Mbp). Orange point, 10 kb bins overlapping with *AFF3* (chr2 bin 100.17–100.18 Mbp). Genomic positions are based on GRCh37/hg19.

(O) Genome-wide effects of siKDM3B, siG9a, and double knockdown on H3K9me2 levels. Scatterplots show all 10 kb bins across the genome, with input-normalized H3K9me2 ChIP-seq densities in two conditions at each bin represented as a point. Left, scatterplot comparing H3K9me2 densities in control vs. siKDM3B. Middle, scatterplot for control vs. siG9a cells. Right, scatterplot for control vs. siKDM3B + siG9a cells. Red lines correspond to >1.5-fold increase or decrease compared with control. Colored points correspond to the bins listed in (N). Red points, 10 kb bins overlapping the central region of KMT2A gene (containing exons 8–14). Green points, 10 kb bins overlapping the 5′ region of KMT2A (exons 1–8). Blue points, 10 kb bins overlapping the 3′ region of KMT2A (exons 14–36). Purple points, 10 kb bins overlapping with *TCF3*. Orange point, 10 kb bin overlapping with *AFF3*. Genomic positions are based on GRCh37/hg19.

Error bars represent the SEM. Asterisk indicates significant difference from indicated ($p < 0.05$) by two-tailed Student's t test. A minimum of 2 replicates per experiment were conducted. For FISH, a minimum of 200 nuclei were scored per replicate per experiment. BA, break aparts. NS, not significant to control.

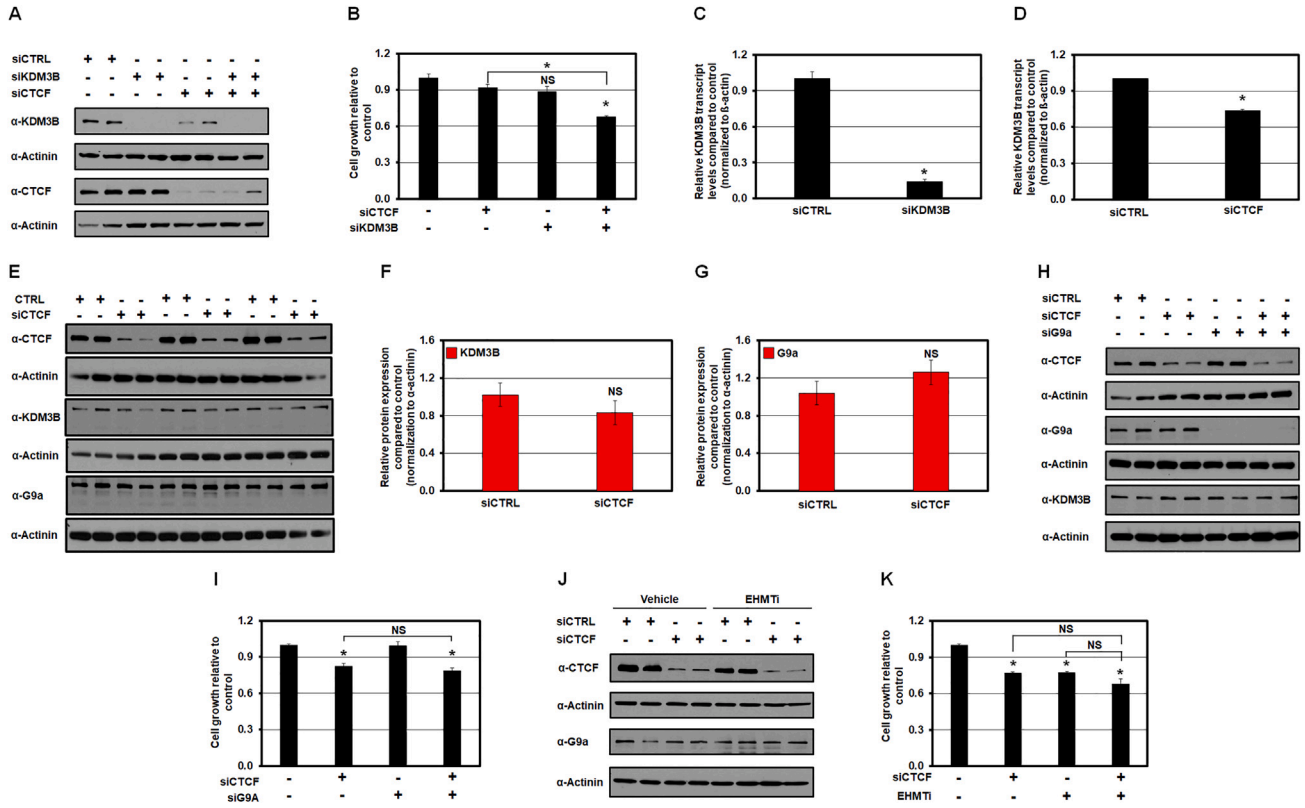

Figure S5. Reduced CTCF occupancy leads to *KMT2A* copy gains and break aparts, related to Figure 5

(A) Western blot validating siRNA depletion of KDM3B and CTCF in RPE cells.

(B) Cell growth assays for siRNA KDM3B and/or CTCF co-depletion in RPE cells.

(C) RT-qPCR analysis of KDM3B transcript levels relative to β-actin upon KDM3B siRNA depletion in RPE cells. Corresponding to Figures 5D and 5E.

(D) RT-qPCR analysis of KDM3B transcript levels relative to β-actin upon CTCF siRNA depletion in RPE cells from three independent experiments.

(E) Western blot for three independent experiments evaluating CTCF, KDM3B, and G9a protein levels in cells siRNA depleted for CTCF.

(F) Western blot quantification of KDM3B protein in (E) that was normalized to α-actinin.

(G) Western blot quantification of G9a protein in (E) that was normalized to α-actinin.

(H) Western blot demonstrating siRNA depletion of CTCF and G9a.

(I) Cell growth assays for siRNA CTCF and/or G9a/EHMT2 co-depletion.

(J) Western blot demonstrating siRNA depletion of CTCF and relative protein level expression of G9a after EHMTi treatment.

(K) Cell growth for siRNA CTCF depletion and/or EHMTi-treated cells.

Error bars represent the SEM. Asterisk indicates significant difference from indicated ($p < 0.05$) by two-tailed Student's t test. A minimum of 2 replicates per experiment were conducted.

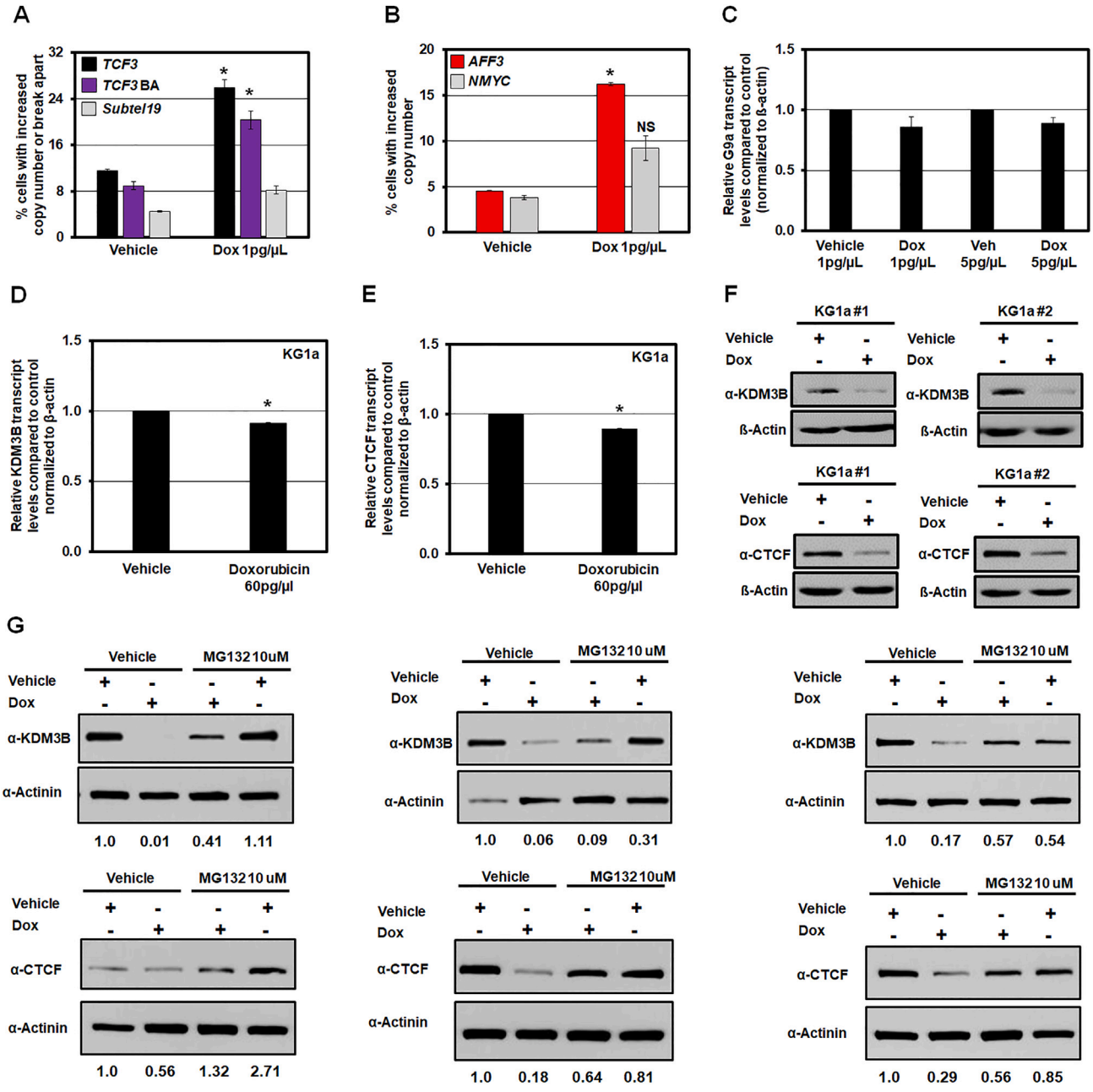

Figure S6. Doxorubicin promotes *KMT2A* amplification and rearrangement and reduces KDM3B and CTCF protein levels, related to Figure 6

(A) Graph of DNA FISH quantification for RPE cells treated with 1 pg/µL Dox for 72 h. Dox treatment causes significant copy gains and break aparts at the *TCF3/E2A* locus, while the control region (*Subtel19*) did not have significant change.

(B) Graph of the DNA FISH quantification for RPE cells treated with 1 pg/µL Dox for 72 h. Dox treatment causes significant copy gains *AFF3/LAF4* locus, while the control region (*NMYC*) was not significant.

(C) RT-qPCR of G9a transcript levels in RPE cells after 72 h of Dox. Samples were normalized to β-actin.

(D) RT-qPCR analysis demonstrating that Dox modestly but significantly reduced *KDM3B* transcript levels relative to β-actin in KG1a cells.

(E) RT-qPCR analysis demonstrating that Dox modestly but significantly reduced *CTCF* transcript levels relative to β-actin in KG1a cells.

(F) Western blots of two independent experiments illustrating Dox reducing KDM3B (top) and CTCF (bottom) protein levels in KG1a cells.

(G) Western blots illustrating MG132 partial rescue of KDM3B (top) and CTCF (bottom) protein levels of individual experiments. Quantification of protein levels of KDM3B (top) or CTCF (bottom) normalized to α-actinin is below each blot. These quantifications were used to generate the avg. ratio shown in Figures 6L and 6M. Representative images used in Figures 6L and 6M are on the far right.

Error bars represent the SEM. Asterisk indicates significant difference from indicated ($p < 0.05$) by two-tailed Student's t test. A minimum of 2 replicates per experiment were conducted. For FISH, a minimum of 200 nuclei were scored per replicate per experiment. BA, break aparts. NS, not significant to control.

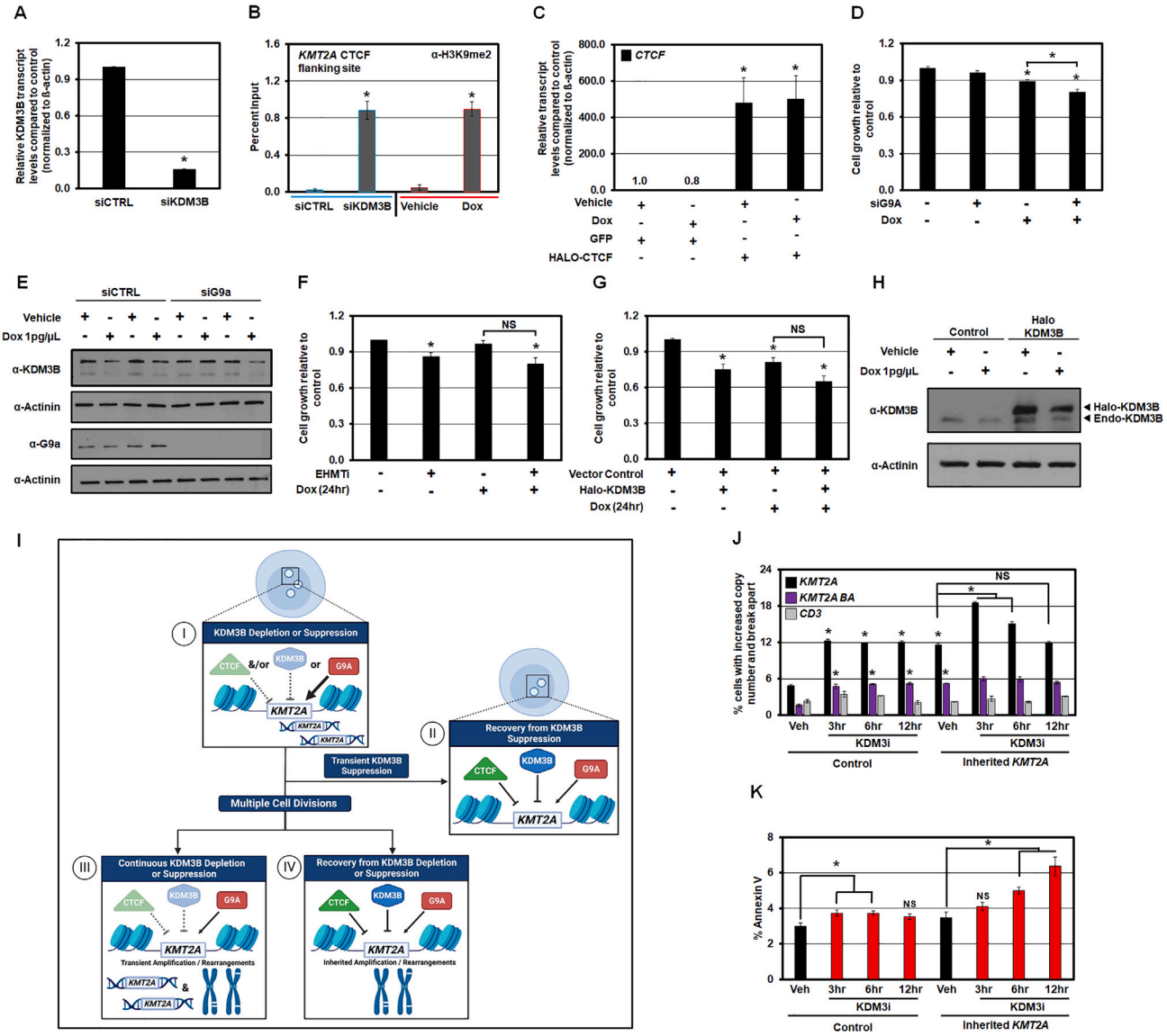

Figure S7. KDM3B and CTCF regulation controls doxorubicin-induced *KMT2A* amplification and rearrangement, related to Figure 7

(A) Graph of the RT-qPCR validation for siKDM3B-mediated depletion of RPE cells. Samples used in (B) and Figure 7A. Samples were normalized to β-actin.

(B) ChIP-qPCR demonstrating an increase of H3K9me2 at *KMT2A* (*KMT2A* CTCF flanking site) following KDM3B siRNA depletion (left; blue) and Dox treatment at 1 pg/μL for 24 h (right; red).

(C) Graph of the RT-qPCR validation for Halo-CTCF overexpression and 24-h doxorubicin treatment in RPE cells. Samples were normalized to β-actin.

(D) Graph of the cell growth assays for siRNA-mediated G9a depletion with or without Dox treatment for 24 h.

(E) Western blot demonstrating siRNA-mediated depletion of G9a and Dox treatment. Dox treatment alone does not impact G9a protein levels.

(F) Graph of the cell growth assays for Dox and/or EHMTi-treated RPE cells for 24 h.

(G) Graph of the cell growth assays with or without Dox treatment for 24 h and/or KDM3B overexpression in RPE cells.

(H) Western blot illustrating overexpression of HALO-KDM3B (left) and HALO-CTCF (right) in RPE cells. Dox reduced both exogenous Halo-tagged (upper band) and endogenous (lower band) KDM3B and CTCF protein levels.

(I) A schematic depicting the regulation of *KMT2A* DNA copy gains and rearrangements. KDM3B and/or CTCF control *KMT2A* copy gains and break aparts, while G9a promotes the events (I; Figures 1, 2, 4, and 5). Upon removal of transient suppression of KDM3B (<1 cell cycle), *KMT2A* extrachromosomal DNA copy gains and break aparts recover and return to baseline (II; Figure 2F). With longer suppression of KDM3B (multiple cell cycles), *KMT2A* copy gains and rearrangement events become inherited in the genome (bottom; Figure 3). Continuous depletion of KDM3B (e.g., *KDM3B* LOH) generates transient extrachromosomal and inherited *KMT2A* amplifications (III; Figure 4D). Recovery from KDM3B depletion or suppression after multiple cell cycles results in inherited *KMT2A* DNA copy gains as rearrangements, which cannot be removed or rescued (IV; Figure 4E).

(J) DNA FISH quantification for inherited *KMT2A* RPE cells generated in Figure 3F, treated with KDM3i for 3–12 h. Inherited *KMT2A* cells have a significant increase in *KMT2A* copy number after 3 and 6 h of KDM3i exposure. No increase in *KMT2A* copy number is observed at 12 h.

(legend continued on next page)

(K) Annexin V staining for inherited *KMT2A* RPE cells generated in Figure 3F, treated with KDM3i for 3–12 h. Longer exposure to KDM3i results in increased apoptosis for the inherited *KMT2A* cells, but not the control cells.

Error bars represent the SEM. Asterisk indicates significant difference from indicated ($p < 0.05$) by two-tailed Student's t test. A minimum of 2 replicates per experiment were conducted. For FISH, a minimum of 200 nuclei were scored per replicate per experiment. BA, break aparts. NS, not significant to control.